Static magnetic signature of a ghost-ship propulsor system as a composite ferromagnetic medium

R. Zivieri ✉ ⓘ ; G. Palomba ⓘ ; G. Consolo ⓘ ; E. Proverbio ⓘ

Check for updates

View Online

Export Citation

CrossMark

04 November 2023 19:11:03

Static magnetic signature of a ghost-ship propulsor system as a composite ferromagnetic medium

View Online   Export Citation   CrossMark

R. Zivieri,[1,a] [ID] G. Palomba,[1] [ID] G. Consolo,[2] [ID] and E. Proverbio[1] [ID]

AFFILIATIONS

[1] Department of Engineering, University of Messina, Contrada di Dio, 98166 Messina, Italy

[2] Department of Mathematical, Computer, Physical and Earth Sciences, University of Messina, Contrada di Dio, 98166 Messina, Italy

[a] Author to whom correspondence should be addressed: roberto.zivieri@unife.it

ABSTRACT

In this paper, it is shown that the static magnetic signature of a propulsor belonging to a ghost ship, whose hull is made of fiberglass, can be calculated by regarding it as a composite ferromagnetic medium. The calculation of the magnetic signature in the static regime is carried out using finite-element method simulations and according to a simple analytical model based on the concepts of volume averaged magnetization arising from a source magnetic field, volume averaged permeability, surface magnetic charges, and the demagnetization tensor applied to a composite magnetic medium. Using targeted simulations, it is demonstrated that the magnetostatic field of demagnetizing nature forming inside the propulsor almost cancels the contribution of the volume averaged magnetization. From the interplay between the numerical simulations and the analytical model, the elements of the demagnetization tensor in the region filled by the propulsor are locally calculated, and their role in determining the localization effects of the magnetic signature is discussed. By replacing the original ferromagnetic materials with weakly ferromagnetic ones, it is shown that, in the underwater region outside the propulsor, the magnetic signature drop is 64%. This analysis suggests an experimental way to use a simple passive method to minimize the magnetic signature of a propulsor as an alternative to more complex and time-consuming methods, such as the deperming and degaussing methods, widely employed to reduce the magnetic signature of ships and underwater objects in military applications.

I. INTRODUCTION

It is well-known that the term *signature* has been associated, in the first place, with the acoustic measurement and detection of a vessel's underwater sound pressure field.[1,2] The underwater sound produced by a ship has characteristics that are unique to it and can be used to distinguish it from others. Even though a surface ship's or submarine's magnetic field is not as unique as its corresponding acoustic field, the term signature has been extended to describe the spatial and temporal distribution of a ship's electromagnetic fields. To quantify the magnetic sources of ships, these systems can be regarded both as magnetic and electric dipole moments. In addition to the most relevant magnetic dipole contribution induced by the earth's magnetic field, which can be detected and accurately

measured by advanced sensor systems with different geometries (such as different types of magnetometers, both of classical and quantum type[3–15]), non-negligible magnetic signature contributions also arise from magnetic fields of electric origin, such as those caused by eddy currents, corrosion currents, and currents flowing in the internal circuits.[9,16–18] Therefore, the characterization of the main sources of magnetic signatures in ships and vessels is crucial, especially for their detection and identification. To obtain that, in the first place, first-principle models consisting of analytical calculations supported by numerical analyses have been developed. In a typical calculation, the geometry of a ship, the magnetic permeability, and the magnitude and direction of the earth's magnetic field contribute to the induction of magnetic signatures are key ingredients. First-principle models allow calculating the magnetic signatures of

a moving object based on magnetic scale models. The starting point is to characterize the magnetic sources and choose the most appropriate system of reference, which depends on the object's shape. It should be remarked that, among all these sources, the hull of a ship or of a small-sized vessel is in most cases ferromagnetic (e.g., steel) and makes an important contribution to the magnetic signature. However, even when the hull is not ferromagnetic, there are other magnetic field signatures inside the ship that contribute to the total magnetic field signature.

A general issue regarding ships and underwater objects is that the underwater magnetic signature is often high and must be reduced[18–21] to make their detection and localization quite complicated. In this respect, active or passive methods are generally employed to reduce the magnetic signature of ships and underwater objects. Active methods consist of different types of degaussing, a process made to decrease or eliminate the magnetic signature of a magnetized object by generating an artificial distribution of magnetic flux density,[18,19] or a re-degaussing process when a part of the degaussing coils is not operable.[20] This artificial distribution of magnetic flux density has intensity and geometry equal to and opposite to the source magnetic signature. Two types of degaussers are utilized: electromagnetic, which uses electrical charges passing through degaussing coils, and permanent magnets, which are made by rare earth magnets. In all cases, the superposition of the compensated and uncompensated fields results in a very low magnetic signature. On the other hand, passive methods include the use of materials with low permeabilities and deperming techniques, the latter consisting of successive hysteresis loops able to demagnetize typical ferromagnetic materials.[21] In addition, magnetic shielding is another method that can be regarded both as active and passive and was applied to shield structures at extremely low frequencies. In this context, analytical and numerical solutions were found for highly conductive and ferromagnetic materials, showing their different shielding behaviors.[22]

For ships and vessels, magnetic signatures resulting from roll and pitched-induced eddy currents,[16,17,23] corrosion currents, and currents flowing in the internal circuits[16,17] might be considerable. In this respect, ship magnetization numerical modeling to evaluate the magnetic signature of a ship taking the simple form of a hollow cylinder[24] and a quantitative analysis of the field radiated by an electrical propulsor motor generating a magnetic induction on the order of about 10^5 nT close to the motor together with a comparison of the numerical results with signature measurements[25,26] have been carried out. In both cases, for the numerical simulations, one of the first released versions of the finite element method (FEM) software, called Flux3D, has been used.

The present analysis focuses on the calculation of the magnetic signature of a ghost-ship in the static regime. Therefore, the magnetic signatures due to eddy currents, corrosion currents, and internal circuit currents can be safely neglected. Furthermore, since the hull of the ghost-ship here considered is made of fiberglass, i.e., a non-magnetic material, the magnetic signature due to the dipole source induced by the earth's magnetic field vanishes. Therefore, the only appreciable contribution to the magnetic signature results from the permanent ferromagnetism of its main propulsor system. The aim of this work is to compute and minimize this type of signature by regarding the propulsor as a composite ferromagnetic medium via (1) the formulation of a simple analytical model based on the definition of volume averaged magnetization and permeability and on the application of the demagnetization tensor formalism to a macroscopic object of a few meters of size, and (2) carrying out FEM simulations on the composite ferromagnetic system through the creation of a mesh of tetrahedral elements of different sizes for the whole propulsor and the region outside it. The interplay between the analytical results and the results of the simulations has allowed us to determine the local numerical values of the demagnetizing elements for this type of composite ferromagnetic medium. This combined analysis has allowed achieving the following two objectives: (i) the calculation of the external and internal static magnetic signatures of the ghost-ship propulsor system immersed in water; and (ii) the proposal of a simple passive method to reduce the magnetic signature in the static regime in the water region surrounding the propulsor system and the quantification of this signature reduction. The first goal was accomplished by considerably simplifying the original propulsor system, keeping only the components contributing for the most part to the magnetic signature, whereas the second one was carried out via the targeted replacement of some Original Ferromagnetic Materials (OFMs) composing the propulsor system with Weakly Ferromagnetic Materials (WFMs). In addition, this material substitution was performed by describing the whole propulsor system as a composite ferromagnetic system having volume averaged magnetic properties. Note that, in all the analyses, the propeller is
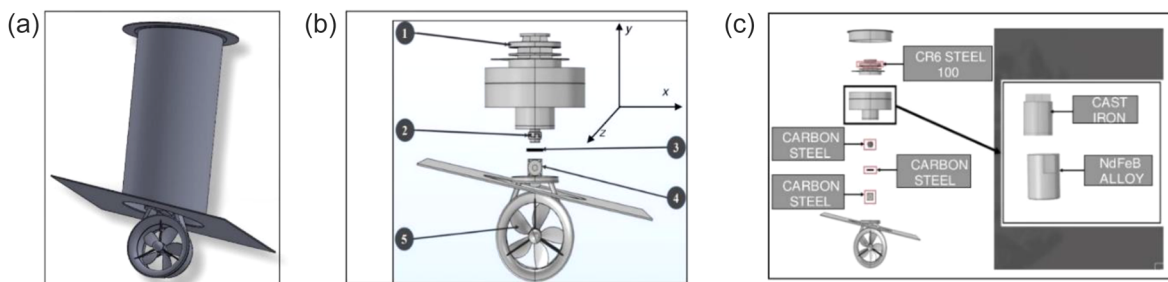
FIG. 1. (a) Schematics of the *in-house*-designed propulsor. (b) Simplified version of the propulsor showing the main components here retained: (1) rotating head bearing; (2) coupling between gear and the electric motor; (3) cooling drive pulley; (4) right-angle head; and (5) propeller. (c) Details of the materials for the components listed in (b) with the inclusion of the ones for the electric motor.

TABLE I. Main technical characteristics of the propulsor.

Technical characteristics of the propulsor	Value
Mass	3320 Kg
Volume	0.98 m^3
Height	4.60 m
Propeller diameter	0.86 m
Hub diameter	0.19 m
Top coverage area	3.14 m^2
Side coverage area	10.20 m^2
Connecting plate	9.86 m^2

always included in the propulsor system. By regarding the propulsor as a composite ferromagnetic system, there are two main advantages: (i) there is a better characterization of the magnetic signature based on a targeted substitution of the materials constituting the propulsor itself, and (ii) the numerical calculations are simplified via the introduction of volume averaged quantities, a volume averaged magnetization, and permeability resulting from the weighted averages of the saturation magnetizations and of the relative permeabilities of the materials, respectively.

The paper is organized as follows. In Sec. II, the analytical model and the numerical approach performed by using FEM software are presented. Section III discusses the results of the analysis, their physical implications, and the interplay between the analytical and numerical results. In Sec. IV, conclusions are drawn.

II. MODELING AND METHODS

The analysis carried out aims at determining and minimizing the static magnetic signature of a standard, *in-house*-designed propulsor of a ghost-ship like the one shown in Fig. 1(a). Therefore, the magnetic field due to eddy currents, corrosion currents, and internal current flowing in the internal circuits of the ship related to the dynamic regime can be neglected and is not included in the calculations. Since the hull of the ghost-ship under consideration is made of fiberglass, a non-magnetic material, the relevant part of the magnetic signature comes from the contribution resulting from the ferromagnetic parts of the propulsor contained in the ship and

supposed to be underwater. The analysis was based on numerical simulations whose input parameters were determined according to a simple analytical model. In the following, it is first described the simulation framework, then the analytical model and its interplay with the numerical simulations.

A. Simulations framework

The static magnetic signature of the propulsor system has been determined by considering it as a composite magnetic medium via the definition of a volume weighted averaged magnetization and a volume weighted averaged permeability. This definition was applied taking into account the saturation magnetizations and the relative permeabilities of every component of the propulsor weighted by their relative volumes.

To maximize the efficiency of the numerical model and reduce the computational time, a simplified version of the propulsor system has been considered, taking into account only the relevant components of the propulsor that contribute to the magnetic signature [see Figs. 1(b) and 1(c)]. The origin of the reference frame has been placed in correspondence with the coupling between gear and the electric motor. The magnetic signature of the smallest components has been neglected, being at least one order of magnitude less than that of the relevant ones. The main components of the propulsor considered in the simplified numerical model are represented in Fig. 1(b) (together with the reference frame) and consist of (1) rotating head bearing, (2) coupling between gear and the electric motor, (3) cooling drive pulley, (4) right-angle head, and (5) propeller. The materials constituting them are specified in Fig. 1(c), including the ones of the synchronous electrical motor made by both $Nd_2Fe_{14}B$ permanent magnets and iron and the motor coating made by cast iron. Note that, in addition to the contribution of the mentioned components, the influence of both the electrical motor and the motor coating on the magnetic signature is remarkable. The mass and the geometric dimensions of the components are summarized in Table I.

The static magnetic signature of the propulsor system has been calculated using the finite-element software (FEM) COMSOL MULTIPHYSICS.[27] FEM simulations have been performed to build up a control volume made up of a cubic box of $10 \times 10 \times 10$ m^3 containing the propulsor system, as shown in Fig. 2(a). The mesh of the cubic box is constituted by tetrahedral non-structural elements having sides between 0.18 and 1 m, whereas those used to simulate
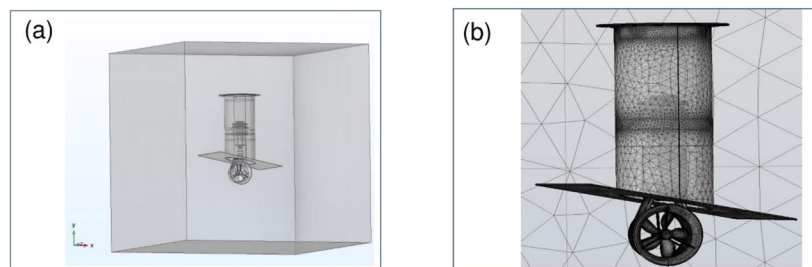
FIG. 2. (a) Cubic simulation box $10 \times 10 \times 10$ m^3 containing the propulsor and the propeller. (b) Tetrahedral non-structural elements of the mesh distributed in the cubic box and in the propulsor system.

the propulsor have sides between 0.1 and 0.8 m, depending on the considered part of the propulsor [see Fig. 2(b)].

B. Analytical model

Simulations have been carried out in the magnetostatic limit, that is, neglecting the time variations of the electric field, and in a current-free region, i.e., $\mathbf{J} = \mathbf{0}$ with $\mathbf{J}$ the current density. In this limit, the Ampère circuital law in differential form for a ferromagnet reads $\nabla \times \mathbf{H}_m = \mathbf{0}$, where $\mathbf{H}_m = (H_{m\,x}, H_{m\,y}, H_{m\,z})$ is the magnetostatic field, a conservative vector that can be thus expressed in terms of the gradient of a scalar magnetic potential Φ_m, namely $\mathbf{H}_m = -\nabla\Phi_m$. In the simulations, the Gauss law $\nabla \cdot \mathbf{B} = \mathbf{0}$, with $\mathbf{B} = -\mu_0 \nabla\Phi_m$ the magnetic induction and μ_0 the vacuum permeability, has also been considered.

It is useful to subdivide the region filled by the cubic box into two regions: (i) an *inner region*, filled by the propulsor constituted by ferromagnetic materials and characterized by a static magnetization; and (ii) an outer non-magnetic region, supposed to be totally filled by water.

In the *inner region*, the volume averaged magnetization has been defined in a rectangular reference frame as $\langle\mathbf{M}\rangle_V = \langle M_x\rangle_V \hat{i} + \langle M_y\rangle_V \hat{j} + \langle M_z\rangle_V \hat{k}$ with

$$\langle M_x\rangle_V = \frac{M_x^{(ci)}V^{(ci)} + M_x^{(pm)}V^{(pm)} + M_x^{(s)}V^{(s)}}{V}, \quad (1a)$$

$$\langle M_y\rangle_V = \frac{M_y^{(s)}V^{(s)}}{V}, \quad (1b)$$

$$\langle M_z\rangle_V = \frac{M_z^{(ci)}V^{(ci)} + M_z^{(pm)}V^{(pm)}}{V}, \quad (1c)$$

where the superscripts "(ci)," "(pm)," and "(s)" are the symbols used for cast iron, permanent magnets, and steel, respectively, and $V = V^{(ci)} + V^{(pm)} + V^{(s)}$ is the total volume. In the special case studied here, the permanent magnets are made of a special iron alloy, the $Nd_2Fe_{14}B$ alloy. In the calculation of $\langle\mathbf{M}\rangle_V$, the ferromagnetism of the soft iron of the stator and the rotor of the synchronous electric motor has been absorbed into one of the permanent magnets. Indeed, the corresponding volume is small and negligible if compared to that of the other parts of the system. Due to the different spatial orientations of the parts composing the propulsor system, the contributions to the volume averaged magnetization components expressed in Eq. (1) are different [see Figs. 1(a) and 1(b)].

The constitutive relation in terms of the volume averaged magnetization is expressed as $\mathbf{B}_{in} = \mu_0(\mathbf{H}_{m\,in} + \langle\mathbf{M}\rangle_V)$ with $\mathbf{B}_{in} = (B_{in\,x}, B_{in\,y}, B_{in\,z})$ the resulting nonuniform magnetic induction within the propulsor system, $\langle\mathbf{M}\rangle_V = (\langle M_x\rangle_V, \langle M_y\rangle_V, \langle M_z\rangle_V)$ is the volume averaged magnetization of the propulsor system uniformly distributed and defined in Eq. (1), and $\mathbf{H}_{m\,in} = (H_{m\,in\,x}, H_{m\,in\,y}, H_{m\,in\,z})$ is the nonuniform magnetostatic field due to the non-ellipsoidal shape of the propulsor system. The field $\mathbf{H}_{m\,in}(x, y, z)$ has a demagnetizing nature and is calculated from the magnetostatic scalar potential Φ_m, $\mathbf{H}_{m\,in} = -\nabla\Phi_m$ being $\Phi_m = \Phi_m(x, y, z)$.

By using the constitutive relation and the definition of $\mathbf{H}_{m\,in}$, the well-known flux conservation law can be rewritten in terms of the volume averaged magnetization as

$$\nabla \cdot \left(\nabla\Phi_m - \langle\mathbf{M}\rangle_V\right) = 0. \quad (2a)$$

Equation (2a) can be cast in the form of a Poisson equation

$$\nabla^2\Phi_m = \langle\rho_m\rangle_V, \quad (2b)$$

with $\langle\rho_m\rangle_V = \nabla \cdot \langle\mathbf{M}\rangle_V$, which represents a volume averaged magnetic charge density expressed as the divergence of the volume averaged magnetization.

By assuming that $\langle\mathbf{M}\rangle_V$ is uniformly distributed throughout the propulsor system, the surface solution in the presence of a contour surface, represented in this case by the surface of the propulsor system, reads

$$\Phi_m(\mathbf{r}) = \int_V \nabla' \frac{1}{|\mathbf{r} - \mathbf{r}'|} d\mathbf{r}' \cdot \langle\mathbf{M}\rangle_V, \quad (3)$$

where we have taken into account the divergence theorem $\int_S \frac{\mathbf{n}\cdot\langle\mathbf{M}\rangle_V}{|\mathbf{r}-\mathbf{r}'|} dS' = \int_V \nabla' \frac{1}{|\mathbf{r}-\mathbf{r}'|} dV' \cdot \langle\mathbf{M}\rangle_V$ with $\mathbf{r} = (x, y, z)$ and $\mathbf{r}' = (x', y', z')$ and $\mathbf{n} \cdot \langle\mathbf{M}\rangle_V$, the volume averaged surface magnetic charge density generated on the propulsor surface by $\langle\mathbf{M}\rangle_V$.

The nonuniform magnetostatic field generated by the volume averaged surface magnetic charge density $\mathbf{H}_{m\,in} = -\nabla\Phi_m$ is obtained from Eq. (3) and, up to first-order terms of demagnetizing effects,[28] reads $\mathbf{H}_{m\,in} = -\underline{\underline{N}}\,\langle\mathbf{M}\rangle_V$ with $\underline{\underline{N}} = \underline{\underline{N}}(x, y, z)$, the point function first-order demagnetization tensor giving a demagnetizing nature to the magnetostatic field inside the propulsor and locally opposite to the static magnetization. In general, for uniformly magnetized bodies of different shapes, the demagnetization tensor is a real and symmetric second-rank tensor with non-negative diagonal elements ($0 \leq N_{ii} \leq 1$ with $i = x, y, z$), and the point-function diagonal components are non-negative obeying the sum rule $N_{xx}(x, y, z) + N_{yy}(x, y, z) + N_{zz}(x, y, z) = 1$ or $\text{tr}(\underline{\underline{N}}) = 1$ with tr denoting the trace[28,29] according to a general theorem valid for both the point-function and the magnetometric demagnetization tensor.[28–34] In vector form, the magnetic induction resulting from the volume averaged magnetization can be thus expressed as

$$\mathbf{B}_{in} = \mu_0\left(\underline{\underline{I}} - \underline{\underline{N}}\right)\langle\mathbf{M}\rangle_V, \quad (4)$$

with $\underline{\underline{I}}$ the 3×3 identity matrix.

The demagnetizing effect incorporated in $\mathbf{H}_{m\,in}$ almost totally cancels the contribution due to the magnetization leading to a very low $\mathbf{B}_{in}$ intensity. For the non-ellipsoidal geometry under study, the point-function demagnetization tensor, via the symmetry condition $N_{ij} = N_{ji}$, reads

$$N_{ij} = \begin{bmatrix} N_{xx} & N_{xy} & N_{xz} \\ N_{xy} & N_{yy} & N_{yz} \\ N_{xz} & N_{yz} & N_{zz} \end{bmatrix}, \quad (5)$$

with $N_{ij} = N_{ij}(x, y, z)$ and, in principle, with non-vanishing off-diagonal components N_{ij} ($i \neq j$). Therefore, the components of the magnetic induction written in compact form read

$$B_{in\,i} = \mu_0(I_{ij} - N_{ij})\langle M_j\rangle_V, \quad (6)$$

where $i, j = x, y, z$, and the summation over the repeated index j has been omitted due to the Einstein summation convention. Looking

at Eq. (6), each component of the magnetic induction depends on all the components of the volume averaged magnetization.

In the proposed model, another physical quantity directly related to the volume averaged magnetization has been introduced: the volume averaged permeability. The volume averaged magnetization can be thought of as originating from a source uniform magnetic field H_s such that $\langle \mathbf{M} \rangle_V = \langle \chi \rangle_V \, \mathbf{H}_s$. In terms of magnitude, $\langle M \rangle_V = \langle \chi \rangle_V \, H_s$ with $\langle \chi \rangle_V$ being the volume averaged magnetic susceptibility and the volume averaged permeability $\langle \mu \rangle_V = \langle \chi \rangle_V + 1$ defined as

$$\langle \mu \rangle_V = \frac{\mu_r^{(ci)} V^{(ci)} + \mu_r^{(pm)} V^{(pm)} + \mu_r^{(s)} V^{(s)}}{V}, \tag{7}$$

with μ_r the relative permeability of the considered material. Taking into account that $\langle \mu_V \rangle \gg 1$, so that $\langle \mu \rangle_V \approx \langle \chi \rangle_V$, we end up with $\langle \mathbf{M} \rangle_V \approx \langle \mu \rangle_V \, \mathbf{H}_s$ ($\langle M \rangle_V \approx \langle \mu \rangle_V \, H_s$), and the magnetic induction [Eq. (4)] can be rewritten in the *inner region* as a quantity proportional to the source field in the approximated form, namely

$$\mathbf{B}_{in} \approx \mu_0 \langle \mu \rangle_V \left(\underline{\underline{I}} - \underline{\underline{N}} \right) \mathbf{H}_s. \tag{8}$$

Equation (8) shows that $\mathbf{B}_{in}$ approximately scales linearly with $\langle \mu \rangle_V$, because of the introduction of the source field $\mathbf{H}_s$. Owing to this description, it is also possible to define the magnetostatic energy density $W = W(x, y, z)$ of the propulsor in its general form as

$$W = -\frac{\mu_0}{2} \langle \mathbf{M} \rangle_V \cdot \mathbf{H}_{m\,in}. \tag{9a}$$

The energy density W can be expressed either in terms of the volume averaged magnetization or as a function of the source magnetic field that generates $\langle \mathbf{M} \rangle_V$ itself. In the former case, taking into account that $\mathbf{H}_{m\,in} = -\underline{\underline{N}} \langle \mathbf{M} \rangle_V$, simple calculations lead to

$$W = \frac{\mu_0}{2} N_{ij} \langle M_i \rangle_V \langle M_j \rangle_V. \tag{9b}$$

The magnetostatic energy density of Eq. (9b) has the same form as the energy density entering the magnetostatic self-energy of the uniformly magnetized body with $\langle M_i \rangle_V$ ($\langle M_j \rangle_V$) in place of M_i (M_j).[35] W depends quadratically on the components of the volume averaged magnetization, and this dependence is weighted by the demagnetization tensor components.

An approximate expression of W can be deduced, taking additionally into account that $\langle \mathbf{M} \rangle_V \approx \langle \mu \rangle_V \, \mathbf{H}_s$. Similar calculations yield

$$W \approx \frac{\mu_0}{2} \langle \mu \rangle_V^2 N_{ij} H_{s_i} H_{s_j}. \tag{9c}$$

According to Eq. (9c), the magnetostatic energy density of the propulsor system roughly scales as the square of the volume averaged permeability and has a bilinear dependence on the source magnetic field that creates the magnetization distribution on the propulsor itself.

In the *outer region* filled by water (relative permeability $\mu_{r\,water} = 0.999$), it is $\mathbf{M} = \mathbf{0}$, so the magnetic induction takes the simple expression $\mathbf{B}_{out} \approx \mu_0 \mathbf{H}_{m\,out}$, where $\mathbf{H}_{m\,out}$ is the magnetic field of a magnetostatic source originating outside the propulsor from the scalar potential $\Phi_{m\,out}$. This magnetostatic field is subjected to the

flux conservation law expressed as a Laplace equation in terms of the magnetostatic potential, $\nabla^2 \Phi_{m\,out} = 0$. The continuity condition at the border between the *inner region* and the *outer region* ensures that $\mathbf{H}_{m\,out}$ depends on both the volume averaged magnetization and volume averaged permeability defined in the *inner region* so that $\mathbf{B}_{out} = \mathbf{B}_{out} (\langle \mu \rangle_V)$.

Equation (1), the constitutive relation, and Eq. (7) were used to determine the magnetic signature in the *inner region* according to COMSOL simulations. Equation (9a) was used to determine the corresponding energy density.

In the numerical simulations, magnetic insulation has been considered a boundary condition at the boundary between the *inner region* and the *outer region*. This condition consists of setting to zero the normal component of the magnetic induction at the border of the box in the *outer region* filled by water, i.e., $\mathbf{n} \cdot \mathbf{B}_{out} = 0$, being $\mathbf{n}$ the normal unit vector. Moreover, the uniform earth magnetic field has been removed from the total field, so the resulting magnetic signature is the one associated with the permanent magnetism of the ferromagnetic materials constituting the propulsor system.

Two analyses of the magnetic signature have been addressed:

(1) in the presence of the OFMs ($\mu_{r\,i} \gg 1$) and,
(2) with some of the OFMs replaced by WFMs ($\mu_{r\,i} \approx 1$).

In this latter case, the relative permeabilities are changed, but the saturation magnetizations for each material are kept fixed. Indeed, for both types of analyses, the volume averaged magnetization has been calculated according to Eq. (1), taking into account the following materials: (a) carbon steel; (b) AISI 316 L steel; (c) $Nd_2Fe_{14}B$ magnet alloy;[36,37] and (d) cast iron. The $Nd_2Fe_{14}B$ magnet is an artificial permanent magnet made by an alloy of neodymium, iron, and boron forming a tetragonal crystal structure. There can be two forms of $Nd_2Fe_{14}B$: (1) the bonded form and (2) the sintered form. While the bonded magnet is made of rapidly quenched magnetic powder and binder by "compression or injection molding," the sintered one is made by powder metallurgy. Moreover, the two forms also exhibit different static magnetic properties, such as remanence, magnetic coercivity, saturation magnetization, and energy density, which are generally higher when dealing with the sintered form. In the simulations, the $Nd_2Fe_{14}B$ magnet has been assumed in the sintered form considering that permanent magnet motors are built up using this technique (even though permanent magnets in this form have higher processing costs and could experience large losses during processing).

Note that the effect of soft iron, of which the stator and the rotor of the electric motor are made, has not been considered because it has been reasonably supposed that the main contribution to the magnetic signature was given by the permanent magnets that fill the major part of the electric motor. Moreover, the effects of the volume elements that have been discarded because of the simplification of the propulsor have been adsorbed into the magnetizations of the considered materials.

III. RESULTS AND DISCUSSION
A. Simulations results

For both OFM and WFM types of investigations, two setups (A) and (B) have been examined to determine the magnetic signature.

In these setups, the value of the $Nd_2Fe_{14}B$ alloy saturation magnetization is fixed,[38] whereas the saturation magnetization of cast iron and steel, as known, may vary in a wide range.[39,40] For this reason, in setups (A) and (B), the lower and upper extrema of this interval, respectively, have been considered. This choice has been made taking into account that, from a practical point of view, different types of cast iron and steel are chosen to build up propulsor systems as integral parts of ships or underwater objects, thus being characterized by different static magnetic properties. Of course, especially the steel saturation magnetization can take other values ranging between the minimum and maximum values considered here, depending on the type of steel studied, but this change would not affect the general results obtained for the magnetic signature of the propulsor.

Due to the circular symmetry of the propulsor under study, the saturation magnetization of each material has been weighted equally over the two involved components, either x, z or x, y, depending on the geometry of the subpart of the propulsor examined. In particular, the magnetization components assigned to the electric motor are x and z, while the ones assigned to the propeller are x and y due to their different orientations (see Fig. 1). In both setups, the volumes of the three materials considered, namely cast iron, $Nd_2Fe_{14}B$ alloy, and steel are $V^{(ci)} = 0.029$ m³, $V^{(pm)} = 0.080$ m³, and $V^{(s)} = 0.859$ m³, respectively, and the total volume turns out to be $V = 0.968$ m³.

In setup (A), for both OFM and WFM types of investigation, the following saturation magnetizations have been employed: $M^{(ci)} = 0.820 \times 10^6$ A/m and $M^{(s)} = 1.194 \times 10^6$ A/m[39] for high-carbon cast iron and steel, respectively, and $M^{(pm)} = 1.273 \times 10^6$ A/m for the sintered $Nd_2Fe_{14}B$ alloy taken as a permanent magnet.[38] The values of the saturation magnetization components read: $M_x^{(ci)} = M_z^{(ci)} = 0.580 \times 10^6$ A/m; $M_x^{(pm)} = M_z^{(pm)} = 0.900 \times 10^6$ A/m; $M_x^{(s)} = M_y^{(s)} = 0.844 \times 10^6$ A/m. The calculation of the components of the volume averaged magnetization according to Eq. (1) yields: $\langle M_x \rangle_V = 0.841 \times 10^6$ A/m, $\langle M_y \rangle_V = 0.749 \times 10^6$ A/m, and $\langle M_z \rangle_V = 0.092 \times 10^6$ A/m. In this case, the volume averaged magnetization is $\langle M \rangle_V = 1.130 \times 10^6$ A/m, a value clearly greater than $M^{(ci)}$ but slightly lower than $M^{(s)}$ and less than $M^{(pm)}$.

Instead, in setup (B), for both OFMs and WFMs types of investigation, $M^{(ci)} = 1.670 \times 10^6$ A/m and $M^{(s)} = 1.700 \times 10^6$ A/m for low-carbon cast iron and steel, respectively, were employed,[40] and the same value $M^{(pm)} = 1.273 \times 10^6$ A/m as saturation magnetization of the sintered $Nd_2Fe_{14}B$ alloy for permanent magnets. The values of the components of the volume averaged magnetization read: $M_x^{(ci)} = M_z^{(ci)} = 1.180 \times 10^6$ A/m, $M_x^{(pm)} = M_z^{(pm)} = 0.900 \times 10^6$ A/m, and $M_x^{(s)} = M_y^{(s)} = 1.203 \times 10^6$ A/m. The calculation of the saturation magnetization components according to Eq. (1) yields: $\langle M_x \rangle_V = 1.176 \times 10^6$ A/m, $\langle M_y \rangle_V = 1.067 \times 10^6$ A/m, and $\langle M_z \rangle_V = 0.110 \times 10^6$ A/m. The magnitude of the volume averaged magnetization is $\langle M \rangle_V = 1.592 \times 10^6$ A/m, a value slightly less than $M^{(ci)}$, distinctly less than $M^{(s)}$ and clearly greater than $M^{(pm)}$.

The analytically calculated volume averaged magnetization components have been used as input magnetization parameters for COMSOL simulations to calculate the magnetic signature in both types of analysis. In turn, the interplay between the numerical simulations and the analytical model allows the calculation of the magnitude H_s of the source uniform magnetic field, which gives rise

to the volume averaged magnetization. This approach, based on the composite magnetic medium description, also offers the considerable advantage of simulating such a large composed system with an affordable computational time.

First, let us discuss the magnetic signature due to the OFMs. In Table II, the components of the propulsor constituted by the OFMs are summarized, together with the corresponding materials and their relative permeabilities. The corresponding relative permeabilities are $\mu_r^{(ci)} = 600$ for cast iron, $\mu_r^{(pm)} = 360$ for the $Nd_2Fe_{14}B$ alloy of permanent magnets, $\mu_r^{(s)} = 100$ for carbon steel, $\mu_r^{(s,Cr)} = 350$ for 100Cr6 steel, and $\mu_r^{(s,AISI)} = 1.015$ for stainless steel. The volume averaged permeability has been calculated according to Eq. (7) considering, as unique materials with $\mu_r^{(s)} = 100$, the four components: (1) the right-angle head; (2) the coupling between gear and the electric motor; (3) the cooling drive pulley; and (4) the propeller, leading to $\langle \mu \rangle_V^{OFMs} \approx 136$. In this calculation, the same materials and the corresponding volumes employed for the calculation of the volume averaged magnetization were taken into account. In addition, the small contribution to the volume averaged permeability resulting from the rotating head bearing (having a relative permeability $\mu_r^{(s,Cr)} = 350$ but a very small volume if compared to the other components made of steel) and from the remaining parts of the propulsor was neglected.

Like the volume averaged magnetization, the volume averaged permeability also has a value slightly higher than that of the carbon steel permeability. Straightforwardly, the intensity H_s of the source magnetic field creating the volume averaged magnetization amplitude $\langle M \rangle_V$ for the OFMs case can be determined via the relation $H_s \approx \langle M \rangle_V / \langle \mu \rangle_V^{OFMs}$. For example, for setup (A), it is $H_s \approx 0.831 \times 10^4$ A/m, while for setup (B), it is $H_s \approx 1.171 \times 10^4$ A/m. In the volume averaged model, the source magnetic field is reasonably assumed to be constant as it passes from OFMs to WFMs. This has been accomplished by envisioning a rescaling of the volume averaged magnetization, used as an input parameter in the numerical simulations, to the same entity as that experienced by the volume averaged permeability.

The distribution of the magnetic induction on the surface and inside the propulsor (*inner region*), obtained by means of the

TABLE II. List of the various components of the propulsor together with the indication of the materials used in the analysis made with the OFMs. The corresponding relative permeabilities are also shown.[27]

Component	Material	Relative permeability
Right-angle head	Carbon steel	100
Coupling between gear and the electric motor	Carbon steel	100
Rotating head bearing	100 Cr6 steel	350
Cooling drive pulley	Carbon steel	100
Permanent magnets	$Nd_2Fe_{14}B$ alloy	360
Coating electric motor	Cast iron	600
Remaining parts of the propulsor	AISI 316 L steel	1.015
Propeller	Carbon steel	100
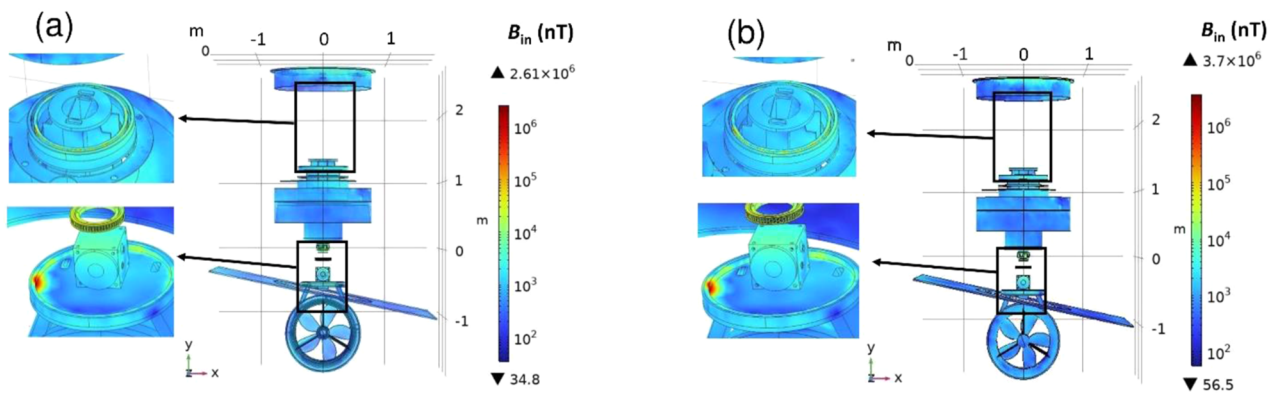
FIG. 3. (a) Distribution of the magnetic induction on the surface and inside the propulsor (*inner region*) obtained in the presence of the OFMs obtained according to setup (A). The regions where the magnetic induction exhibits its maximum values are indicated by the rectangles, and their enlargements are sketched on the left. (b) As in panel (a), but according to setup (B).

simulations, is shown in Fig. 3: panel (a) for setup (A) and panel (b) for setup (B). The magnetic induction (on a logarithmic scale) of the composite ferromagnetic system is not uniform, and B_{in} has a rather low intensity even in the presence of high permeability ferromagnetic materials. The magnetic signature is at least tens or hundreds of nT throughout most parts of the propulsor system, and it is on the order of a few μT in some portions of the motor coating, in the connecting plate above the propeller, and in the propeller but, in some regions, it takes bigger values. Indeed, B_{in} exhibits an intensity peak of a few mT in a narrow region under the left part of the right-angle head component and of hundreds of μT in the external circular region of the rotating head bearing, as shown by the enlarged areas marked by the rectangles and indicated by the arrows on the left of each panel of Fig. 3. The slight nonuniformity trend is attributed to the slight nonuniformity of the magnetostatic field $\mathbf{H}_{m\,in}$ forming inside and on the surface of the propulsor generated by the surface magnetic charges. Surface magnetic charges are due to $\langle \mathbf{M} \rangle_V$, which is locally opposite to $\mathbf{H}_{m\,in}$. The magnetostatic field counterbalances almost completely in several parts of the propulsor the volume averaged magnetization, leading to a strong reduction of the intensity of the magnetic induction and low intensity values in the *inner region* both inside and on the surface of the propulsor. It is interesting to note that in the former case, the peak distribution of B_{in} is asymmetric, while in the latter case, it is almost symmetric with a weak spatial inhomogeneity. The magnetic induction asymmetric distribution observed in the region under the left part of the right-angle head component has no magnetic origin, but it can be attributed to the geometry, which influences the magnitude of the spatially dependent off-diagonal demagnetizing factors appearing in the demagnetization tensor of Eq. (5) (see Sec. III B for further details). Finally, note that, according to setup (B), there is an enhancement of B_{in} of about 60% if compared to B_{in} determined according to setup (A).

In Fig. 4, the calculated components of the magnetostatic field [panels (a), (b), and (c)] and of the magnetic induction [panels (d), (e), and (f)] for setup (A) refer to the rectangular reference frame employed in the numerical simulations. Each component of the magnetostatic field takes a negative sign opposite to that of the
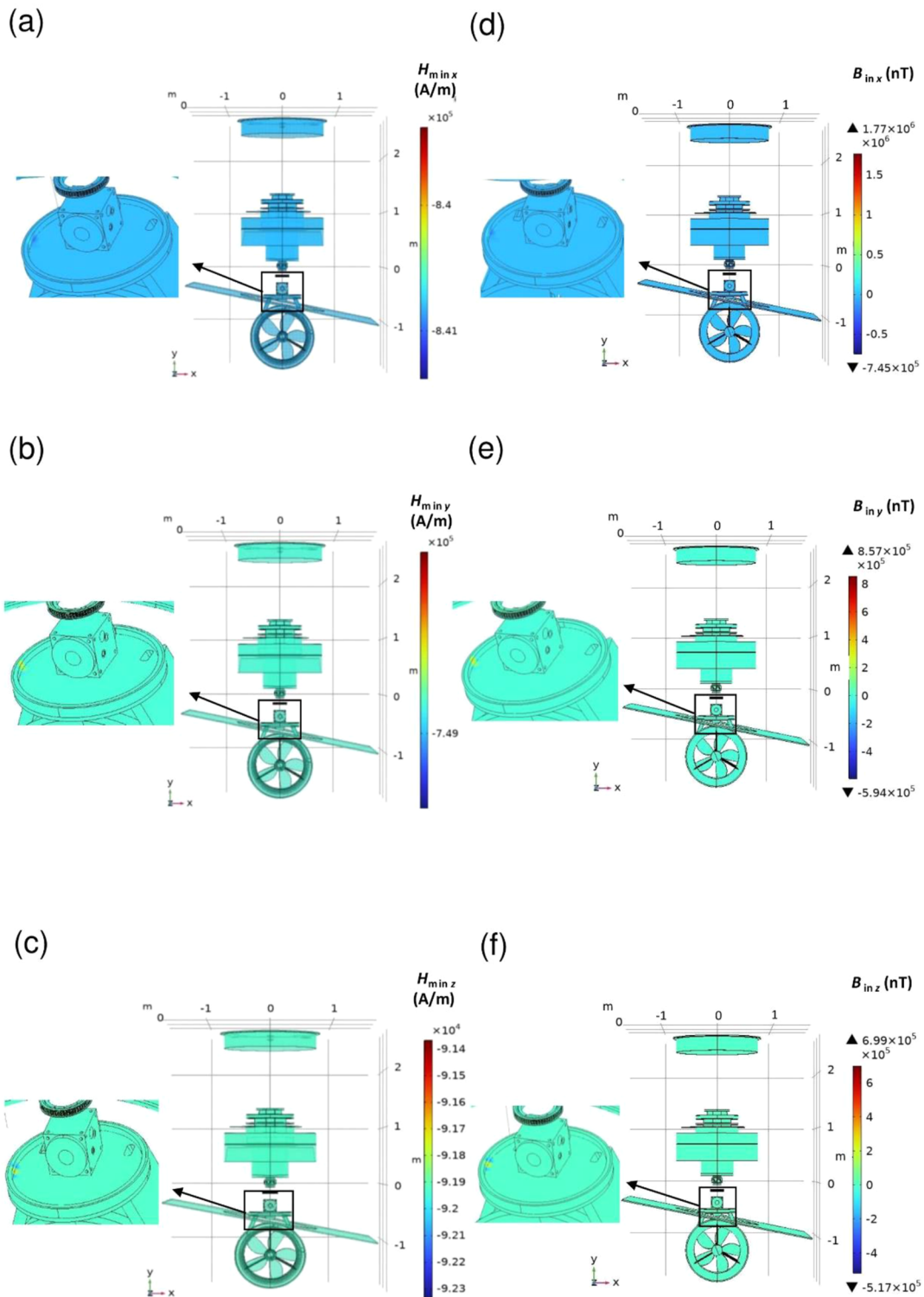
volume averaged magnetization, confirming the demagnetizing nature of the volume averaged magnetostatic field in the *inner region*. The magnetostatic field components are weakly nonuniform and exhibit their highest values in the region under the left part of the right-angle head component [see the enlarged area at the left of panels (a), (b), and (c)], and this localization is more accentuated for the $H_{m\,in\,z}$ component.

The components $H_{m\,in\,x}$ and $H_{m\,in\,y}$ are equal and opposite to $\langle M_x \rangle_V$ and $\langle M_y \rangle_V$, respectively, while $H_{m\,in\,z}$ is almost equal and opposite to $\langle M_z \rangle_V$ depending on the part of the propulsor considered, and the corresponding components of the magnetic induction also assume negative values. This means that the point-function off-diagonal components of the demagnetization tensors $N_{xy}(x, y, z)$, $N_{xz}(x, y, z)$, and $N_{yz}(x, y, z)$ also play an important role within the domain filled by the propulsor system (see Sec. III B for a more detailed discussion). Each component of $\mathbf{B}_{in}$ [Figs. 4(d)–4(f)] exhibits its maximum value with similar features to those of $\mathbf{H}_{m\,in}$ components in the region under the left part of the right-angle head component [as shown by the enlarged areas on the left of panels (d), (e), and (f)] as a consequence of the slight spatial nonuniformity of the magnetostatic field components with special regard to the $H_{m\,in\,z}$ component having a more accentuated spatial variation [enlarged areas on the left of panels (a)–(c)].

Similar conclusions about the trend of the magnetostatic field components and of the magnetic induction components can be drawn by analyzing the results of setup (B) summarized in Fig. 5. In this case, the magnetostatic field components assume greater values if compared to the corresponding ones in setup (A) because of the higher volume averaged magnetization. As a general consideration, for both analyses, the magnetostatic field (apart from the sign) is about two orders of magnitude larger than the source magnetic field H_s, and the lower value of this latter is ascribed to the huge magnitude of the volume averaged permeability.
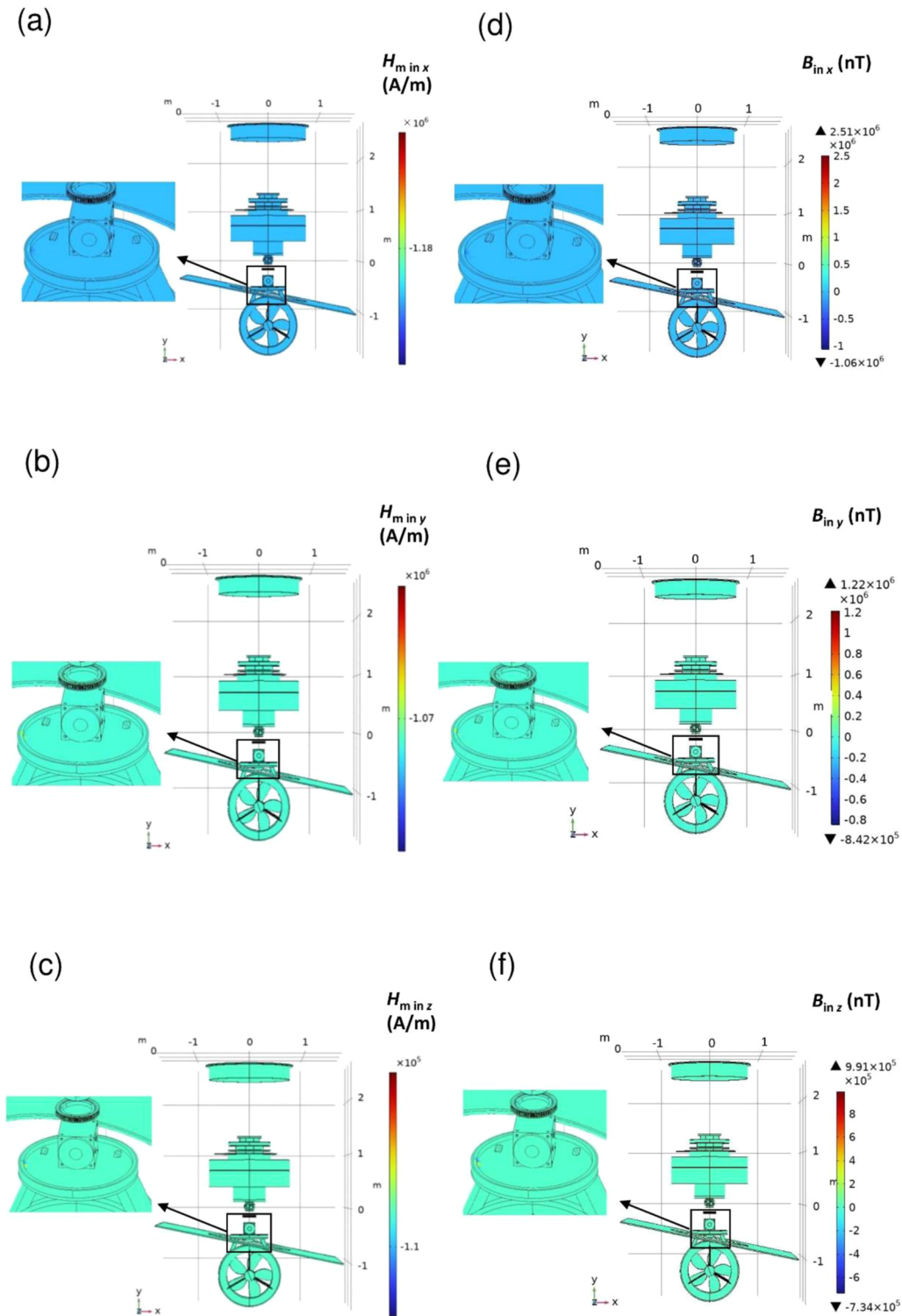
Let us discuss the case made by replacing some of the OFMs with WFMs having $\mu_r \approx 1$ and the effects on the magnetic induction due to this replacement. The components, the corresponding materials, and the relative permeabilities are summarized in Table III. The volume averaged permeability, calculated according to Eq. (3)

04 November 2023 19:11:03

FIG. 4. Distribution of the magnetostatic field and of the magnetic induction components on the surface and inside the propulsor (*inner region*) obtained in the presence of the OFMs according to setup (A). In detail: (a) $H_{m\,in\,x}$; (b) $H_{m\,in\,y}$; (c) $H_{m\,in\,z}$. The region where each component of the magnetostatic field exhibits its maximum value is indicated by the rectangle, and its enlargement is sketched on the left of each panel. (d) $B_{in\,x}$; (e) $B_{in\,y}$; (f) $B_{in\,z}$. The region where each component of the magnetic induction exhibits its maximum value is indicated by the rectangle, and its enlargement is sketched on the left of each panel.

FIG. 5. Distribution of the magnetostatic field and of the magnetic induction components on the surface and inside the propulsor (*inner region*) obtained in the presence of the OFMs according to setup (B). In detail: (a) $H_{m\,in\,x}$; (b) $H_{m\,in\,y}$; (c) $H_{m\,in\,z}$. The region where each component of the magnetostatic field exhibits its maximum value is indicated by the rectangle, and its enlargement is sketched on the left of each panel. (d) $B_{in\,x}$; (e) $B_{in\,y}$; (f) $B_{in\,z}$. The region where each component of the magnetic induction exhibits its maximum value is indicated by the rectangle, and its enlargement is sketched on the left of each panel.

TABLE III. List of the various components of the propulsor together with the indication of the materials used in the analysis made with some of the OFMs substituted with the WFMs. The corresponding relative permeabilities are also shown.[27]

Component	Material	Relative permeability
Right-angle head	AISI 316 L steel	1.015
Coupling between gear and the electric motor	AISI 316 L steel	1.015
Rotating head bearing	AISI 316 L steel	1.015
Cooling drive pulley	AISI 316 L steel	1.015
Permanent magnets	$Nd_2Fe_{14}B$ alloy	360
Coating electric motor	Cast iron	600
Propeller	AISI 316 L steel	1.015
Remaining parts of the propulsor	AISI 316 L steel	1.015

with $\mu_r^{(s)} = 100$ and $\mu_r^{(s,Cr)} = 350$ replaced by $\mu_r^{(s,AISI)} = 1.015$ and using the same assumptions made for the analysis with OMFs, reads $\langle\mu\rangle_V^{WFMs} = 49$.

The volume averaged permeability strongly lowers passing from the OFMs case to the WFMs case so that $\langle\mu\rangle_V^{WFMs}/\langle\mu\rangle_V^{OFMs} = 0.36$. Note that, in the simulations, the reduction of the volume averaged permeability due to the substitutions summarized in Table III has been indirectly introduced by rescaling by 64% the volume averaged magnetization under the reasonable assumption that the source magnetic field intensity $H_s = \langle M\rangle_V/\langle\mu\rangle_V$ generating the volume averaged magnetization would remain constant passing from the OFMs to the WFMs case.

The calculated distribution of the magnetic induction on the propulsor for the WFMs case is depicted in Fig. 6. In panel (a) are shown the results according to setup (A), while in panel (b) are displayed the results obtained according to setup (B). In the WFMs case, the distribution of B_{in} on the s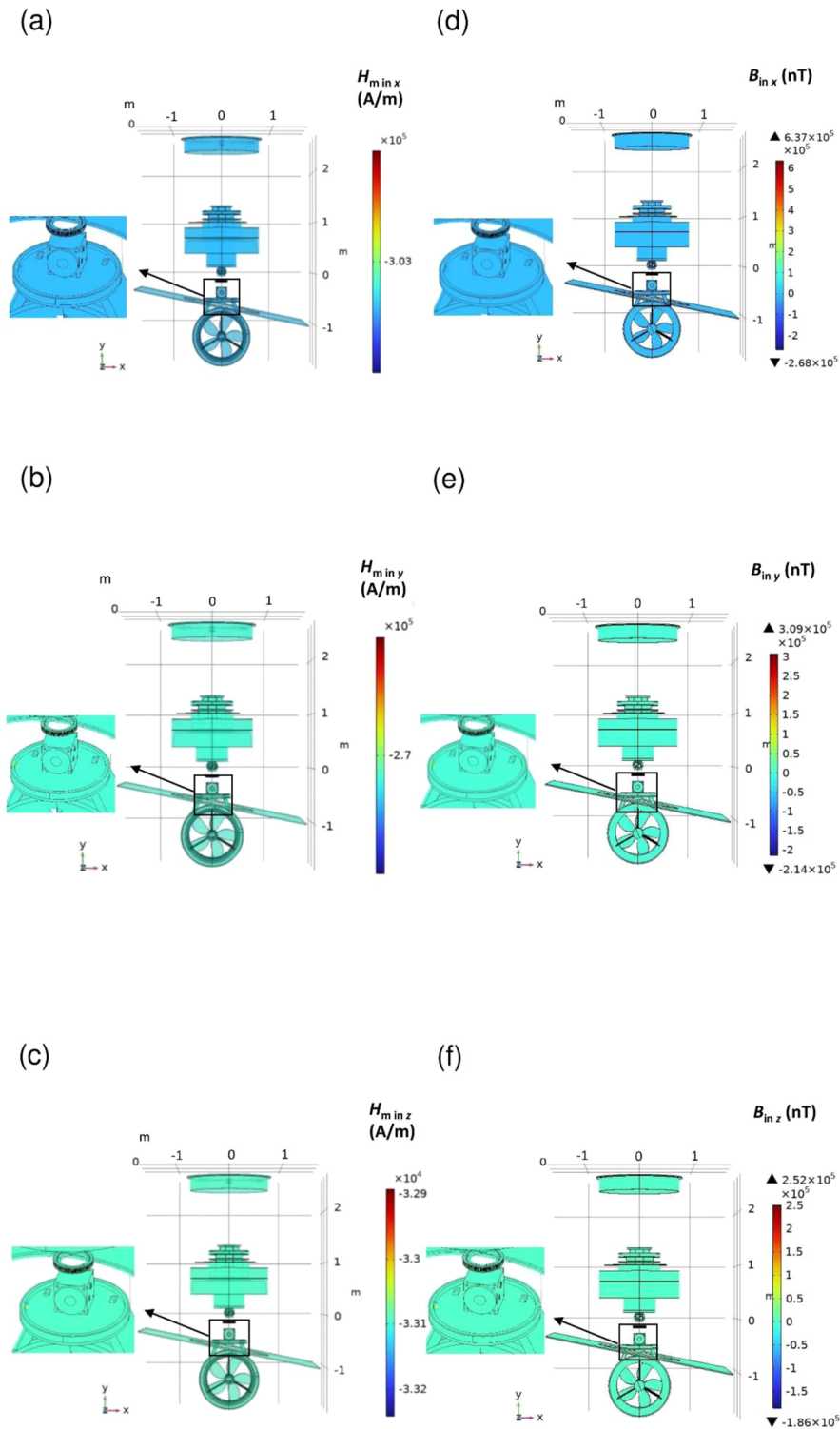urface and inside the propulsor is nonuniform and has very similar features to the ones determined in the OFMs case, as shown in Fig. 3. As expected, also for the WFMs case, the magnetic induction calculated through setup (B) is greater than the corresponding one determined through setup (A) due to the greater values of saturation magnetizations employed for cast iron and steel. For both setups, the magnetic signature reduces by 64% if compared with the corresponding one obtained in the OFMs case [see Figs. 3(a) and 3(b), respectively, for a comparison]. The magnetic signature reduction is in accordance with the reduction experienced by the volume averaged permeability and with Eq. (8) showing that B_{in} linearly scales with $\langle\mu\rangle_V$. Conclusions similar to the ones extracted in the OFMs case regarding the regions where B_{in} has bigger values (see Fig. 3) can be drawn in the WFMs case, as shown by the enlarged areas sketched on the left of panels (a) and (b) of Fig. 6.

In Fig. 7, the distributions on the surface and inside the propulsor of the magnetostatic field components [panels (a), (b), and (c)] and of the magnetic induction components [panels (d), (e), and (f)] that were determined according to setup (A) are displayed. Considerations similar to the ones drawn for the $\mathbf{H}_{m\,in}$ and $\mathbf{B}_{in}$ components in the OFMs case can be made in the WFMs case. The results compared to those summarized in Fig. 4 for the OFMs case indicate that the magnitude of each $\mathbf{H}_{m\,in}$ and $\mathbf{B}_{in}$ component is lower in this latter case. The distribution of the $\mathbf{H}_{m\,in}$ components is rather uniform throughout the propulsor with $H_{m\,in\,z}$ exhibiting a higher degree of nonuniformity albeit being one order of magnitude smaller if compared to $H_{m\,in\,x}$ and $H_{m\,in\,y}$. This difference can be more easily appreciated by looking at the enlarged regions on the left of each panel that exhibit peaks of intensity in the region under the left part of the right-angle head component.
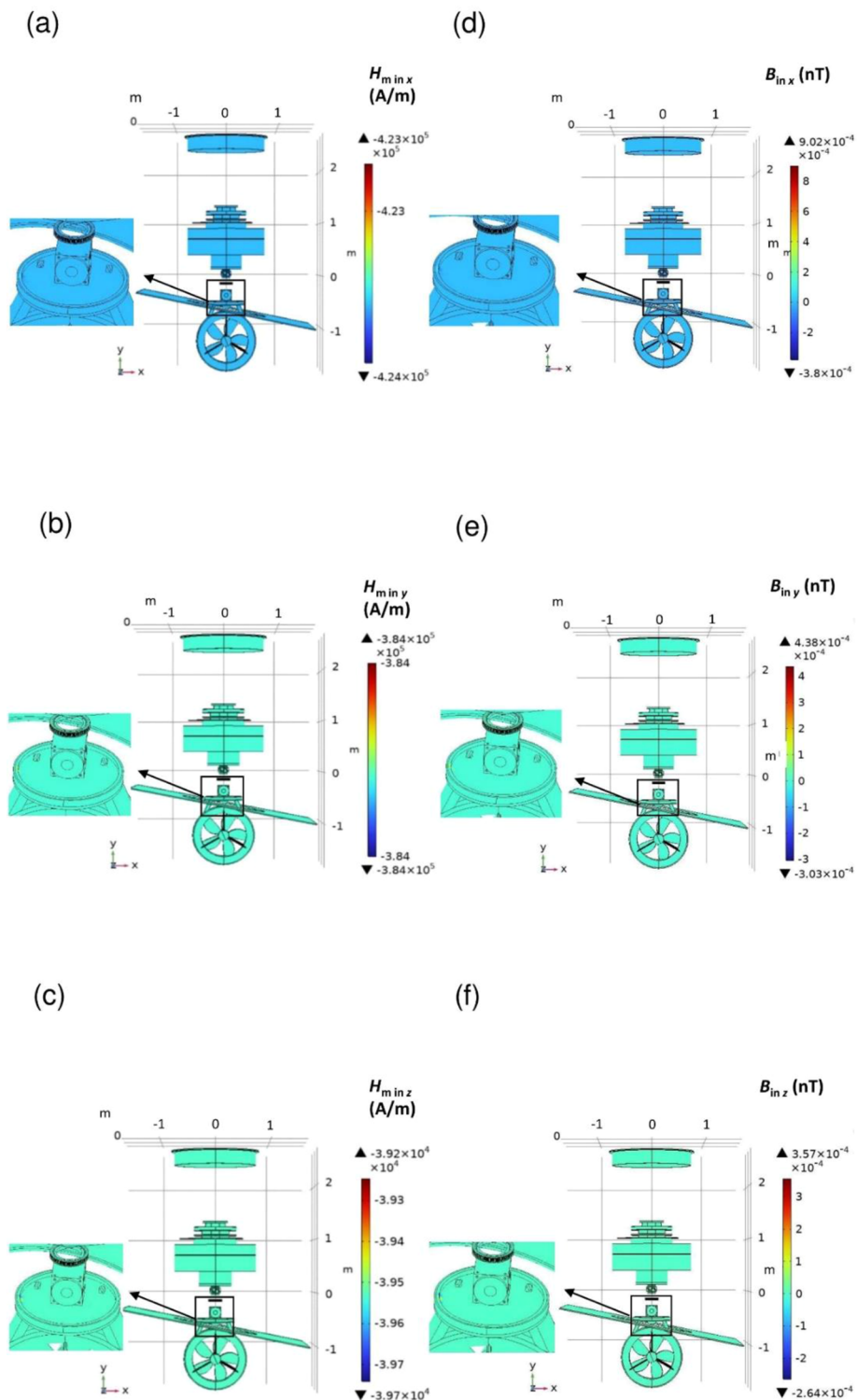
In Fig. 8, the distributions of the $\mathbf{H}_{m\,in}$ and $\mathbf{B}_{in}$ components on the propulsor surface are shown, obtained according to setup (B). A comparison with the distributions displayed in Fig. 5 for the OFMs case confirms that in the WFMs case the magnitudes of the $\mathbf{H}_{m\,in}$ and $\mathbf{B}_{in}$ components are lower, but the localization regions at which the magnetic signature has bigger values are qualitatively the same as for the OFMs case, as shown on the left of each panel.
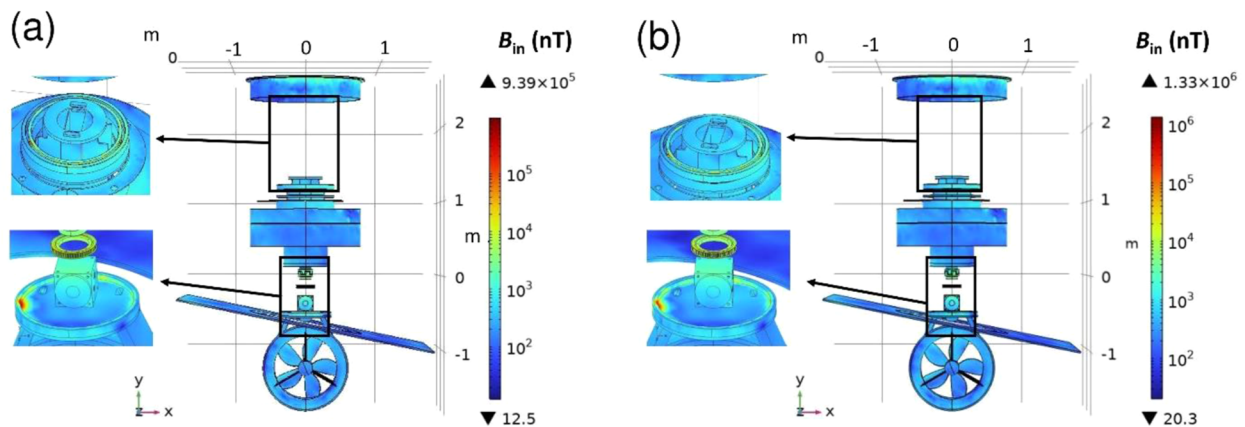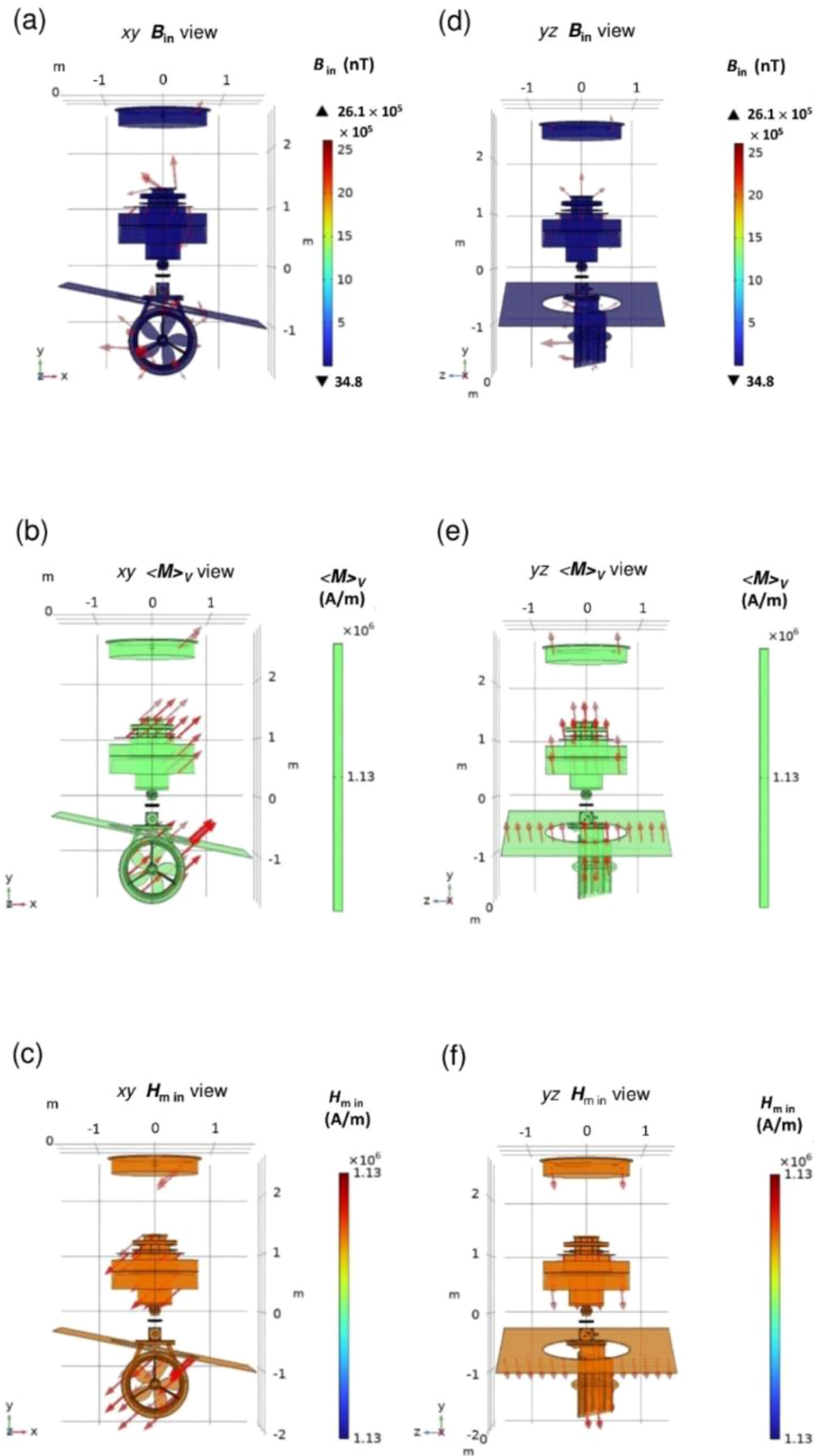

FIG. 6. (a) Distribution of the magnetic induction on the surface and inside the propulsor (*inner region*) obtained in the presence of the WFMs according to setup (A). The regions where the magnetic induction exhibits its maximum values are indicated by the rectangles, and their enlargements are sketched on the left. (b) As in panel (a), but according to setup (B).

FIG. 7. Distribution of the magnetostatic field and of the magnetic induction components on the surface and inside the propulsor (*inner region*) obtained in the presence of the WFMs according to setup (A). In detail: (a) $H_{m\,in\,x}$; (b) $H_{m\,in\,y}$; (c) $H_{m\,in\,z}$. The region where each component of the magnetostatic field exhibits its maximum value is indicated by the rectangle, and its enlargement is sketched on the left of each panel. (d) $B_{in\,x}$, (e) $B_{in\,y}$, (f) $B_{in\,z}$. The region where each component of the magnetic induction exhibits its maximum value is indicated by the rectangle, and its enlargement is sketched on the left of each panel.

04 November 2023 19:11:03

FIG. 8. Distribution of the magnetostatic field and of the magnetic induction components on the surface and inside the propulsor (*inner region*) obtained in the presence of the WFMs according to setup (B). In detail: (a) $H_{m\,in\,x}$; (b) $H_{m\,in\,y}$; (c) $H_{m\,in\,z}$. The region where each component of the magnetostatic field exhibits its maximum value is indicated by the rectangle, and its enlargement is sketched on the left of each panel. (d) $B_{in\,x}$; (e) $B_{in\,y}$; (f) $B_{in\,z}$. The region where each component of the magnetic induction exhibits its maximum value is indicated by the rectangle, and its enlargement is sketched on the left of each panel.

FIG. 9. Vector representation (red arrows) of the magnetic induction, the volume averaged magnetization, and the magnetostatic field. The corresponding intensities distributed on the surface and inside the propulsor are also shown. (a) *xy* view of $\mathbf{B}_{in}$; (b) *xy* view of $\langle \mathbf{M} \rangle_V$; (c) *xy* view of $\mathbf{H}_{m\,in}$; (d) *yz* view of $\mathbf{B}_{in}$; (e) *yz* view of $\langle \mathbf{M} \rangle_V$; (f) *yz* view of $\mathbf{H}_{m\,in}$.

In Fig. 9, the vector distributions of $\mathbf{B}_{in}$ [panels (a) and (d)], $\langle\mathbf{M}\rangle_V$ [panels (b) and (e)], and $\mathbf{H}_{m\,in}$ [panels (c) and (f)] throughout the propulsor are depicted for two different views, along the xy plane and the yz plane, respectively. The calculation has been performed using the magnetic parameters employed in the OFMs case and setup (A), but similar results would be obtained in the other cases investigated. $\mathbf{H}_{m\,in}$ is approximately anti-parallel to the uniform volume averaged magnetization $\langle\mathbf{M}\rangle_V$ in each part of the propulsor including the propeller because of the generation on the propulsor surface of surface magnetic charges, giving $\mathbf{H}_{m\,in}$ a demagnetizing nature and having approximately the same intensity as $\langle\mathbf{M}\rangle_V$. No volume magnetic charges are generated because of the assumed volume averaged magnetization uniformity throughout the propulsor volume. The $\mathbf{H}_{m\,in}$ nonuniformity is weak and, unlike in the component representation, where it is observable, in this analysis, it is completely masked. Taking into account that the magnitude of $\mathbf{H}_{m\,in}$ is comparable to that of $\langle\mathbf{M}\rangle_V$, it is also confirmed that a crucial

role is mainly played by the off-diagonal components and less by the diagonal components of the demagnetization tensor in determining its magnitude (see Sec. III B for further discussion).

The magnetostatic energy density W calculated by means of Eq. (9a) is weakly nonuniform throughout the propulsor surface and inside the propulsor because of the weak nonuniformity of the magnetostatic field. In particular, for the OFMs case, $W = 8.02 \times 10^5$ J/m^3 in setup (A) and $W = 15.9 \times 10^5$ J/m^3 in setup (B). On the other hand, for the WFMs case, $W = 1.04 \times 10^5$ J/m^3 in setup (A) and $W = 2.06 \times 10^5$ J/m^3 in setup (B). For both OFMs and WFMs cases, W experiences an increase of 98% passing from setup (A) to setup (B) due to the higher saturation magnetizations employed in setup (B). Finally, the 87% reduction experienced by W passing from the OFMs to the WFMs case is consistent with the scaling of the magnetostatic energy density as the square of the volume averaged permeability [Eq. (9c)], namely $[\langle\mu\rangle_V^{WFMs}/\langle\mu\rangle_V^{OFMs}]^2 = 0.13$.
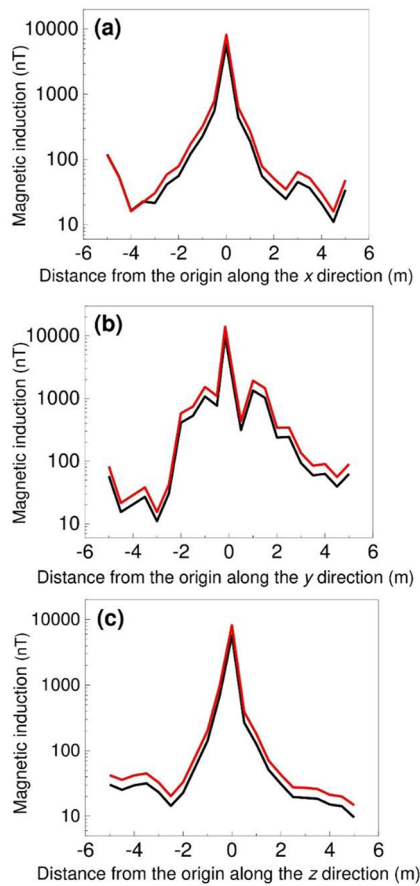
FIG. 10. Magnetic signature as a function of the distance from the propulsor in the presence of the OFMs. (a) Black line: magnetic induction as a function of the distance from the origin of the propulsor along the x direction determined according to setup (A). Red line: magnetic induction as a function of the distance from the origin of the propulsor along the x direction determined according to setup (B). (b) As in panel (a), but along the y direction. (c) As in panel (a), but along the z direction.
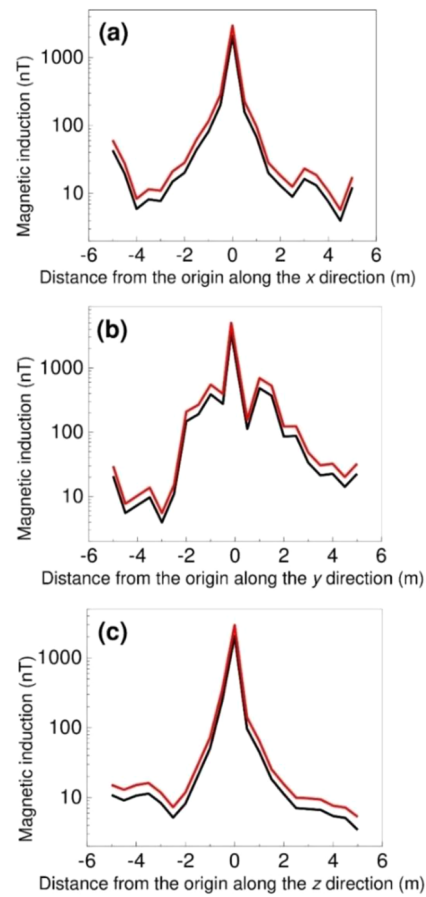
FIG. 11. Magnetic signature as a function of the distance from the origin of the propulsor obtained by substituting some of the OFMs with WFMs. (a) Black line: magnetic induction as a function of the distance from the origin of the propulsor along the x direction determined according to setup (A). Red line: magnetic induction as a function of the distance from the origin of the propulsor along the x direction determined according to setup (B). (b) As in panel (a), but along the y direction. (c) As in panel (a), but along the z direction.

The calculation of the magnetic signature behavior as a function of the underwater distance from the origin of the propulsor system at various distances from the water surface is crucial to understand the magnetic behavior in the region outside the propulsor system itself. The analysis has been carried out along the propulsor axis (y direction) and perpendicularly to the propulsor axis (x and z directions), and in each direction, it includes both spatial values belonging to the *inner region* where $\langle \mathbf{M} \rangle_V \neq \mathbf{0}$ and to the *outer region* where $\langle \mathbf{M} \rangle_V = \mathbf{0}$. In the *outer region*, the magnetic induction depends on the magnetostatic field outside the propulsor, which no longer has a demagnetizing nature and is locally parallel to the magnetic induction. Its magnitude decreases with increasing distance from the propulsor. Note that because of the continuity condition fulfilled by the magnetostatic field across the border between the *inner region* and the *outer region*, which is placed at the surface of the propulsor system, the magnetic signature in the *outer region* still has a dependence on the volume averaged magnetization.

As displayed in Fig. 10, the overall trend of the magnetic signature calculated in the presence of OFMs as a function of the distance along every spatial direction and displayed, for the sake of clarity, on a logarithmic scale is a decreasing function with increasing the distance. The curves obtained in setup (B) (red curves) are slightly upshifted with respect to those determined in setup (A) (black curves) independently of the spatial direction, confirming the influence of a greater volume averaged magnetization. Quantitatively, the difference between the magnetic signature according to setup (A) and setup (B) for fixed values of the distance is not constant for every spatial direction. The non-monotonic behavior is due to the presence of border effects related to the choice of a finite simulation box. The largest values of the magnetic signature are along the propulsor y axis direction at any distance if compared to the ones along the x and z axis directions. Independently of the chosen direction, the magnetic induction exhibits its maximum on the order of thousands of nT and up to 10^4 nT close to the origin of the reference frame, point O = (0, 0, 0 m), placed at the coupling between gear and the electric motor and a few meters underwater. However, note that, from the previous analysis, the magnetic signature at other points of the propulsor not lying along one of the three axes can take values of even a few mT. On the other hand, the magnetic induction at a few meters from the propulsor strongly diminishes becoming on the order of only tens of nT along each direction.
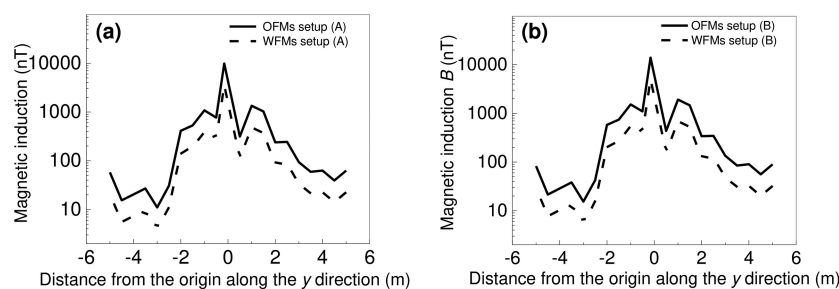
The magnetic induction as a function of the distance from the propulsor obtained with WFMs is displayed in Fig. 11 along the three spatial directions, both for setup (A) (black curves) and setup (B) (red curves). Again, the red curves are slightly upshifted with respect to the black curves, and the upshift is nonuniform as a function of the distance. The strong reduction of the volume averaged permeability obtained by replacing some of the OFMs with WFMs leads to a marked decrease in the magnetic signature. Due to the change in volume averaged permeability, its trend is qualitatively identical to that obtained in the presence of OFMs but, for both setups (A) and (B), the magnitude is lower, being about 1/3 of the one obtained in the presence of the OFMs at any distances reflecting the decrease in volume averaged permeability of 64% and depending on the volume averaged permeability ratio [$\langle \mu \rangle_V^{\text{WFMs}} / \langle \mu \rangle_V^{\text{OFMs}}$ = 0.36]. This value can be obtained by calculating the percentage variation of the magnetic signature (magnetic induction),

$$\Delta B_\% = \frac{B_{\text{WFMs}} - B_{\text{OFMs}}}{B_{\text{OFMs}}} \times 100 = -64\,\%, \tag{10}$$

valid for any directions and any value of the distance considered, independent of the setup analyzed.

In Fig. 12, the magnetic signature as a function of the distance along the y direction obtained in the presence of the OFMs (full black lines) is compared with the one determined by considering the WFMs (dashed black lines). The comparison is made both for setup (A) [panel (a)] and for setup (B) [panel (b)]. The magnetic signature uniformly diminishes by 64% by using the WFMs as a consequence of the same quantitative reduction of the volume averaged permeability. This result corresponds to a strong reduction of the underwater magnetic signature obtained by using a very simple and well-known passive method and facilitated by the composite magnetic medium description of the propulsor system proposed here.

Overall, the drop in the magnetic signature obtained with the passive method under study is not of one order of magnitude as usually occurs with the usual active method such as the degaussing technique and with the passive method such as the deperming technique, but the method here based on the replacement of ferromagnetic materials has the relevant advantages of being less expensive and less time-consuming.

FIG. 12. Comparison between the magnetic signature in the OFMs (full black line) case and in the WFMs (dashed black line) case as a function of the distance along the y direction from the origin of the propulsor for setup (A) [panel (a)] and for setup (B) [panel (b)].

B. Interplay between the numerical simulations and the analytical model: Calculation of the demagnetization tensor components

The aim of this subsection is to present the numerical calculation of the three diagonal components N_{xx}, N_{yy}, and N_{zz} and of the three off-diagonal components N_{xy}, N_{xz}, and N_{yz} of the demagnetization tensor on the surface and inside the propulsor system. This was accomplished by performing an interplay analysis between the simulation results and the analytical model in the *inner region*. Here, the analysis performed in the OFMs case for setup (B) is discussed, but very similar conclusions could be drawn by carrying out the same analysis for setup (A) and for the WFMs case. From the general expression of the magnetic induction [cf. Eq. (6)], the components of $\mathbf{B}_{in}$, by taking into account the symmetry condition of the demagnetization tensor, viz. $N_{ij} = N_{ji}$, take the explicit form

$$B_{in\,x} = \mu_0\big[(1 - N_{xx})\langle M_x\rangle_V - \big(N_{xy}\langle M_y\rangle_V + N_{xz}\langle M_z\rangle_V\big)\big], \quad (11a)$$

$$B_{in\,y} = \mu_0\big[(1 - N_{yy})\langle M_y\rangle_V - \big(N_{xy}\langle M_x\rangle_V + N_{yz}\langle M_z\rangle_V\big)\big], \quad (11b)$$

$$B_{in\,z} = \mu_0\big[(1 - N_{zz})\langle M_z\rangle_V - \big(N_{xz}\langle M_x\rangle_V + N_{yz}\langle M_y\rangle_V\big)\big], \quad (11c)$$

where each component shows a strict dependence on the off-diagonal components of the demagnetization tensor and the spatial dependence has been omitted.

As a preliminary calculation, to fully understand the role of the off-diagonal demagnetization tensor components in the general case studied, three special cases were considered by assuming that the volume averaged magnetization was aligned either along x ($\langle \mathbf{M}\rangle_V = (\langle M_x\rangle_V, 0, 0)$) or along y ($\langle \mathbf{M}\rangle_V = (0, \langle M_y\rangle_V, 0)$) or along z ($\langle \mathbf{M}\rangle_V = (0, 0, \langle M_z\rangle_V)$). In these three special cases, the summation over the repeated indices in $B_{in\,i} = \mu_0(I_{ij} - N_{ij})\langle M_j\rangle_V$ and $H_{min\,i} = -N_{ij}\langle M_j\rangle_V \ \forall \ i, j = x, y, z$ is restricted to only one addendum. At a fixed orientation of the magnetization (either along x or y or z), in these three special cases, the two components of $\mathbf{H}_m$ in depending on the off-diagonal demagnetization tensor components do not vanish and give a small contribution to the total magnetostatic field, as also confirmed by the numerical simulations.

By means of the numerical simulations, it was found that the magnetostatic field $\mathbf{H}_{m\,in}$ is almost opposite to the averaged magnetization $\langle \mathbf{M}\rangle_V$ and has approximately the same intensity. This means that, whatever the direction along which the averaged magnetization lies, the diagonal components of the demagnetization tensor are characterized by very slight local nonuniformities, either $N_{xx} \approx 1$ or $N_{yy} \approx 1$ or $N_{zz} \approx 1$. In this way, it is reproduced, for each direction, a condition similar to that of the magnetostatic field computed in an out-of-plane magnetized thin film lying in the xy plane, composed by three–four monolayers, with the magnetization aligned along the z direction ($N_{zz} = 1$, $N_{xx} = N_{yy} = 0$)[41] basing on a procedure consisting of the direct summation of dipolar fields.[42]

In these three special cases, the components $B_{in\,i}$ are rather small, especially the one depending on the diagonal components N_{ii} of the demagnetization tensor. As a result, magnetic induction depends mainly on its off-diagonal components, N_{ij}. The numerical results of this preliminary calculation are summarized in Fig. 13, where the magnetic signature obtained in the general case [panel (a)]

is compared with those determined in the special cases [panel (c) for the averaged magnetization along x, panel (b) along y, and panel (d) along z] in the region under the right-angle head component. It can be seen that the asymmetry of the distribution of B_{in} in this region, even though, as should be expected, less accentuated with respect to the general case, is present also in these three special cases, especially when the averaged magnetization is aligned either along x or along y. A confirmation of this trend is given by the behavior of the components of B_{in} (not shown), which primarily depend on N_{ij} in the above-mentioned special cases and exhibit an asymmetric distribution in the same region. This key result is proof that the asymmetry of the magnetic signature is mainly due to the off-diagonal components of the demagnetization tensor and, to a lesser extent, to the effect of the diagonal ones.

The analytical 3D system of Eq. (11) consists of three equations and six unknown quantities, the demagnetizing factors, which should be solved locally in the *inner region*. Therefore, due to the unbalancing between the number of equations and the number of unknown quantities, the numerical calculation was carried out basing on an approximated procedure. This procedure consisted of subdividing the analysis into three steps after determining, via numerical simulations, the components of $\mathbf{B}_{in}$ at some representative points of the propulsor system.

First, the diagonal components N_{xx}, N_{yy}, and N_{zz} were calculated. This was accomplished by considering the three 2D equivalent systems of equations: either the simplified Eqs. (11a) and (11b) by setting $H_{m\,z} = 0$ implying $N_{zz} = 0$ but also $N_{xz} = 0$ and $N_{yz} = 0$, or the simplified Eqs. (11a) and (11c) by setting $H_{m\,y} = 0$ implying $N_{yy} = 0$ but also $N_{xy} = 0$ and $N_{yz} = 0$, or the simplified Eqs. (11b) and (11c) by setting $H_{m\,x} = 0$ implying $N_{xx} = 0$ but also $N_{xy} = 0$ and $N_{xz} = 0$ and, for each of the three cases, the corresponding equation given by the sum rule $\mathrm{tr}(N_{ij}) = 1$. In analogy with what occurs in magnetic nanostructures, the vanishing of the ith component of the demagnetizing field ($i = x, y, z$) and of the corresponding diagonal and off-diagonal demagnetizing factors would be obtained by ideally assuming that the size of the system along the ith direction is much greater with respect to the size along the other two spatial directions and that the averaged magnetization is oriented along the ith direction. In this way, the surface magnetic charges created at the borders by the averaged magnetization would be too far away to give rise to a non-vanishing demagnetizing field along the ith direction. The numerical solution of each of the 2D equivalent systems of equations was found by solving simultaneously three equations in three unknown quantities, the two diagonal components (either N_{xx} and N_{yy}, N_{xx} and N_{zz}, or N_{yy} and N_{zz}) and the corresponding off-diagonal component related to the 2D equivalent system under study. N_{zz} was obtained as the average of the two values (almost overlapping) extracted from the two 2D equivalent systems of equations involving this demagnetizing factor.

Second, the numerical values of N_{xx} and N_{yy} obtained by the simplified Eqs. (11a) and (11b) and by the corresponding sum rule $\mathrm{tr}(N_{ij}) = 1$ have been proportionally decreased to adapt them to the case under study: N_{yy} has been decreased by $N_{zz}/2 \times N_{yy}/N_{xx}$, while N_{xx} by $(N_{zz} - N_{zz}/2 \times N_{yy}/N_{xx})$. This operation was performed taking into account the sum rule $\mathrm{tr}(N_{ij}) = 1$ for $i = j = x, y, z$.

Third, the obtained numerical values of N_{xx}, N_{yy}, and N_{zz} were introduced in the system of Eq. (11) under study, and the off-diagonal components N_{xy}, N_{xz}, and N_{yz} were numerically
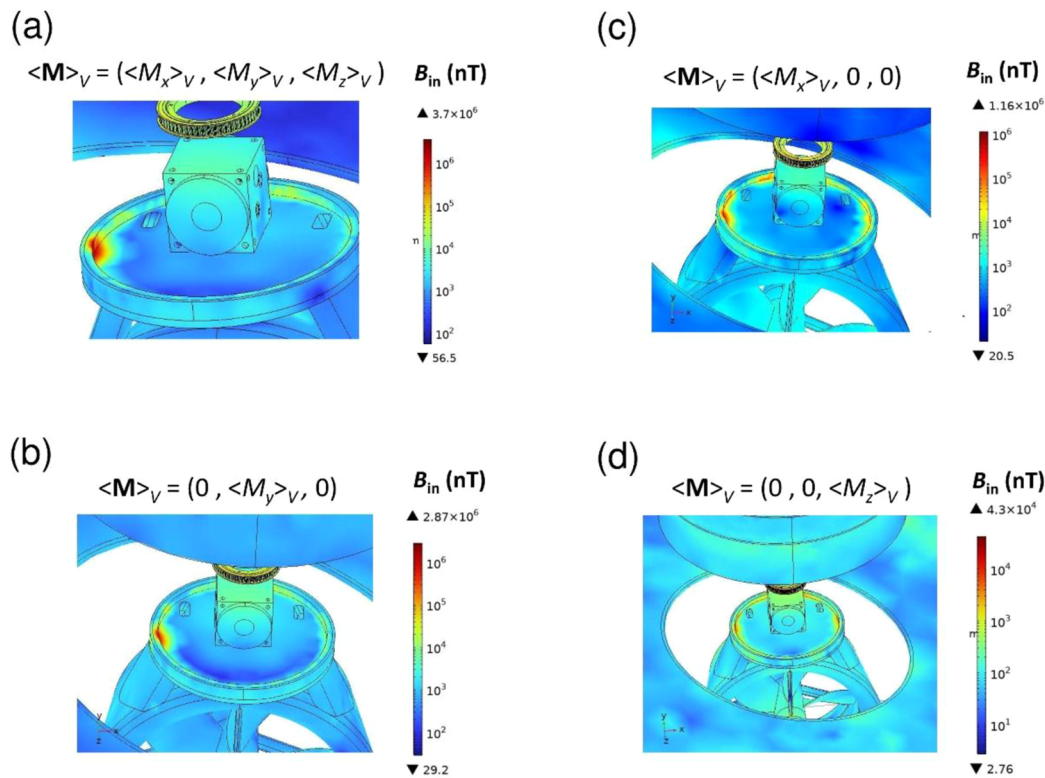
FIG. 13. Distribution of the magnetic induction in the region under the right-angle head component obtained in the presence of the OFMs and according to setup (A), in the general case (a), for $\langle \boldsymbol{M} \rangle_V$ aligned along x (c), along y (b), and along z (d).

determined. The above-mentioned three-step procedure was repeated at the representative points of the propulsor system.

Table IV summarizes the numerical values of N_{xx}, N_{yy}, N_{zz}, N_{xy}, N_{xz}, and N_{yz} at the origin of the propulsor system, $(x, y, z) = (0, 0, 0\ \text{m})$ point, and at specific points belonging to the small regions of the propulsor system at which the magnetic signature takes maximum values. All components take slightly different values at the points considered and show numerical differences at the second decimal place, confirming the weak spatial dependence of the demagnetization tensor for the propulsor system studied here. The N_{xx} and N_{yy} diagonal components are overall almost two orders

of magnitude larger than N_{zz} and, in turn, N_{xx} is bigger than N_{yy}. The off-diagonal component N_{xy} is of the same order of magnitude as N_{xx} and N_{yy}, while the off-diagonal components N_{xz} and N_{yz} are comparable and are one order of magnitude less than N_{xy}.

In this respect, let us consider the $(x, y, z) = (-0.32, -0.50, 0.03\ \text{m})$ point, the central point of the region placed under the left part of the right-angle head component. At this point and in the surrounding region, the magnetic signature is much bigger than in the other parts of the propulsor. Specifically, at this point, $B_{\text{in}} = 1.06 \times 10^6$ nT, a value close to the maximum value $B_{\text{in max}} = 3.7 \times 10^6$ nT (a few μT) observed in adjacent points of the

TABLE IV. Demagnetizing factors at the origin of the reference frame and at four specific points of the propulsor system (*inner region*) corresponding to the maximum values of the magnetic signature. The numerical values of the demagnetizing factors were extracted from the fit to Eq. (11) following the three-step procedure described in the text.

Coordinates (m) (x, y, z)	N_{xx}	N_{yy}	N_{zz}	N_{xy}	N_{xz}	N_{yz}
$(0, 0, 0)$	0.5429	0.4475	0.0096	0.4978	0.0585	0.0376
$(-0.32, -0.50, 0.03)$	0.5441	0.4475	0.0084	0.4973	0.0571	0.0392
$(0.32, -0.50, 0.03)$	0.5429	0.4475	0.0096	0.4978	0.0585	0.0377
$(-0.30, 1.22, 0.16)$	0.5426	0.4477	0.0097	0.4978	0.0594	0.0368
$(0.30, 1.18, 0.16)$	0.5430	0.4474	0.0096	0.4978	0.0598	0.0363

04 November 2023 19:11:03
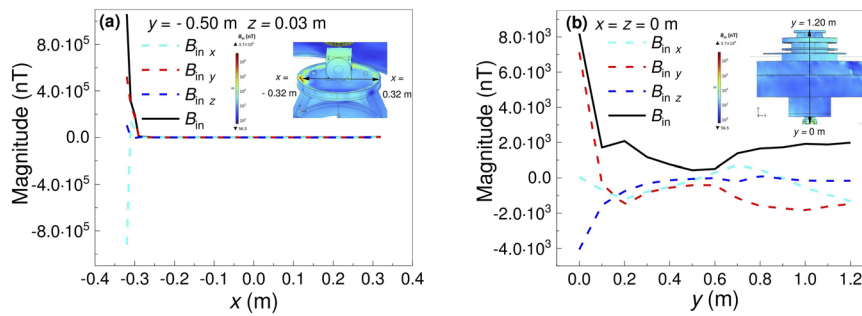
FIG. 14. (a) Behavior of $B_{in\,x}$, $B_{in\,y}$, $B_{in\,z}$, and B_{in} along the x direction inside the propulsor in the region under the right-angle head component in the OFMs case and according to setup (B). The corresponding distribution of the magnetic induction B_{in} in the region of the propulsor system considered together with the x direction is shown. (b) Behavior of $B_{in\,x}$, $B_{in\,y}$, $B_{in\,z}$, and B_{in} along the y direction inside the central part of the propulsor in the region connecting the coupling between gear and the electric motor and the rotating head bearing in the OFMs case and according to setup (B). The corresponding distribution of the magnetic induction B_{in} in the region of the propulsor system considered together with the y direction is also shown.

same region [see the legend of Fig. 3(b)]. At the $(x, y, z) = (0.32, -0.50, 0.03\ \text{m})$ central point of the region placed under the right part of the right-angle head component, the magnetic signature is $B_{in} = 4.82 \times 10^3$ nT; namely, it is three orders of magnitude less than at the $(x, y, z) = (-0.32, -0.50, 0.03\ \text{m})$ symmetric point (with respect to the y axis). An important role (even though not absolute) in determining the big difference in the magnetic signature at the two symmetric points is played by the N_{zz} diagonal component and, to a greater extent, by the off-diagonal components N_{xy} and N_{yz}, which take lower values at the $(x, y, z) = (-0.32, -0.50, 0.03\ \text{m})$ point leading to an overall increase of the magnetic induction at this point. Note that numerical differences in the third decimal place of the demagnetizing factors (see Table IV) could lead to considerable changes in the components of the magnetic induction and, as a result, in B_{in} itself.

Finally, let us discuss the behavior of the components of the demagnetization tensor at the other two selected almost symmetric points (with respect to the y axis) at the centers of the narrow regions belonging to the rotating heading bear, where B_{in} has higher intensity. The two points are placed in the outer part of the rotating heading bear and B_{in} is of comparable intensity: at the $(x, y, z) = (-0.30, 1.22, 0.18)$ point, it is $B_{in} = 4.67 \times 10^5$ nT, and at the $(x, y, z) = (0.30, 1.18, 0.16)$ point, it is $B_{in} = 5.1 \times 10^5$ nT. These values are about one order of magnitude less than the maximum value of B_{in} observed in the region placed under the left part of the right-angle head component. The demagnetizing factors calculated in correspondence of these two almost symmetric points take very close numerical values (see Table IV), leading to magnetic signatures of comparable intensities at these two points. Again, an important role in determining the higher values of the magnetic signature at these two points if compared to other points belonging to the *inner region* is played by the off-diagonal components.

Figure 14(a) displays the magnetic induction components and the magnetic induction as a function of the x coordinate in the region of the propulsor placed under the right-angle head component for $y = -0.50$ m and $z = 0.03$ m together with the spatial distribution of the magnetic induction in this region of the propulsor system. All components of the magnetic induction (dashed lines) exhibit their maximum value in a narrow region around the

$x = -0.32$ m point on the left border, experience a strong decrease just moving away from it and reduce their intensities (apart from the sign) by three orders of magnitude leading to a similar B_{in} reduction. As a comparison, to highlight the main differences in the magnetic signature distribution, Fig. 14(b) shows the components of the magnetic induction and of B_{in} as a function of the y coordinate along the axis of the propulsor system $(x = z = 0\ \text{m})$ in the portion starting from the coupling between gear and the electric motor and ending at the rotating head bearing after crossing the electric motor. One notes that $B_{in\,y}$ and $B_{in\,z}$ are $\sim 10^3$–10^4 nT ($B_{in\,x}$ is smaller) in the whole interval ($0\ \text{m} \leq y \leq 1.20\ \text{m}$) and that B_{in} is maximum at $y = 0$ m reaching almost 10^4 nT ($B_{in} = 8.19 \times 10^3$ nT), and attains a minimum at $y = 0.50$ m in the region filled by the electric motor while still preserving the same order of magnitude. The spatial distribution of the magnetic induction in this central part of the propulsor system is also depicted.

IV. CONCLUSIONS

In this work, the magnetic signature of a propulsor system placed in a ghost ship was calculated in the static regime by using a finite-element method. This numerical approach was based on a simple analytical model, according to which the propulsor was regarded as a composite magnetic system. To reduce the computational cost, a targeted simplification of the original propulsor system was made by properly removing some components whose contributions to the magnetic signature are negligible. The propulsor was regarded as a composite magnetic system characterized by a volume averaged magnetization arising from a source magnetic field and a volume averaged permeability that are close to those of carbon steel, the most representative material constituting the propulsor. The composite magnetic system was also characterized by a magnetostatic field of demagnetizing nature and a spatially varying magnetic induction. In this way, the propulsor system was described as being composed of only one material that incorporates the magnetic and geometric properties of all the different ferromagnetic materials. This description allowed carrying out an interplay between the results of the numerical simulations and the analytical model through the determination of the demagnetizing factors,

which have been shown to strongly affect the spatial behavior of the magnetic signature in the *inner region* filled by the propulsor system and can partially explain the localization effects. According to the numerical results, which give a magnetic signature on average of tens of thousands of nT in the proximity of the propulsor, the propulsor system can be classified as a low signature magnetic system.

The proposal of treating the propulsor as a composite system enabled not only the easy determination of the distribution of the magnetic signature on the propulsor system and inside it but also the computation in a more efficient way of the reduction of the magnetic signature via the replacement of some of the original ferromagnetic materials with weakly ferromagnetic materials. This method, based on material replacement, is less invasive and has a considerable advantage if compared to the usual active method, based on the degaussing process, which implies the use of coils outside the ship to compensate the magnetic signature and also to the other widely employed passive method based on the deperming process, which would be much more elaborate and time consuming. A generalization of this analysis could be the investigation of the dynamic regime of the propulsor system via the extension of the composite system description to the other magnetic sources, such as the signatures due to the eddy currents and the corrosion currents resulting from the internal currents inside the ship and from the currents in the water.

AUTHOR DECLARATIONS

Conflict of Interest

The authors have no conflicts to disclose.

Author Contributions

R. Zivieri: Conceptualization (equal); Data curation (equal); Formal analysis (equal); Investigation (equal); Software (equal); Writing – original draft (equal); Writing – review & editing (equal). **G. Palomba**: Software (equal). **G. Consolo**: Data curation (equal); Funding acquisition (equal); Software (equal); Supervision (equal); Validation (equal); Writing – review & editing (equal). **E. Proverbio**: Funding acquisition (equal); Supervision (equal).

DATA AVAILABILITY

The data that support the findings of this study are available from the corresponding author upon reasonable request.

REFERENCES

[1] M. F. McKenna, D. Ross, S. M. Wiggins, and J. A. Hildebrand, "Underwater radiated noise from modern commercial ships," J. Acoust. Soc. Am. **131**, 92 (2012).

[2] K. Abrahamsen, "The ship as an underwater noise source," Proc. Meet. Acoust. **17**, 070058 (2012).

[3] A. Sheinker, L. Frumkis, B. Ginzburg, N. Salomonski, and B.-Z. Kaplan, "Magnetic anomaly detection using a three-axis magnetometer," IEEE Trans. Magn. **45**, 160–167 (2009).

[4] J. Lenz and S. Edelstein, "Magnetic sensors and their applications," IEEE Sens. J. **6**, 631–649 (2006).

[5] J. E. Lenz, "A review of magnetic sensors," Proc. IEEE **78**, 973–989 (1990).

[6] *Magnetic Sensors and Magnetometers*, edited by P. Ripka (Artech, New York, 2001).

[7] P. P. Ripka and K. Zavěta, "Chapter three magnetic sensors: principles and applications," in *Handbook of Magnetic Materials*, edited by K. H. J. Buschow (Elsevier, Amsterdam, Holland, 2009), Vol. 18, pp. 347–420.

[8] P. Ripka, "Sensors based on bulk soft magnetic materials: Advances and challenges," J. Magn. Magn. Mater. **320**, 2466–2473 (2008).

[9] R. Zivieri *et al.*, "Latest generation quantum effect magnetometry for submarine detection," CMRE-MR-2019-021, 2019.

[10] S. M. Faris and E. A. Valsamakis, "Resonances in superconducting quantum interference devices-SQUIDs," J. Appl. Phys. **52**, 915–920 (1981).

[11] M. Hirota, T. Furuse, K. Ebana, H. Kubo, K. Tsushima, T. Inaba, A. Shima, M. Fujinuma, and N. Tojyo, "Magnetic detection of a surface ship by an airborne LTS SQUID MAD," IEEE Trans. Appl. Supercond. **11**, 884–887 (2001).

[12] M. Hirota, K. Nanaura, Y. Teranishi, and T. Kishigami, "SQUID gradiometers for a fundamental study of underwater magnetic detection," IEEE Trans. Appl. Supercond. **7**, 2327–2330 (1997).

[13] J. Sefati Markiyeh, M. R. Moniri, and A. R. Monajati, "Detection of magnetic anomaly using total field magnetometer," Int. J. Adv. Res. Electr. Electron. Instrum. Eng. **4**, 1813–1820 (2015).

[14] E. Paperno, I. Sasada, and E. Leonovich, "A new method for magnetic position and orientation tracking," IEEE Trans. Magn. **37**, 1938–1940 (2001).

[15] Y. Shangguan, J. Yuan, and J. Zou, "A localization method for submarines based on array probes magnetic measurement at two positions to overcome the influence of background field," Int. J. Appl. Electromagn. Mech. **55**, 205–212 (2017).

[16] J. J. Holmes, *Exploitation of a Ship's Magnetic Field Signatures*, 1st ed. (Morgan & Claypool Publishers, San Rafael, CA, 2006).

[17] J. J. Holmes, *Modeling a Ship's Ferromagnetic Signatures*, 1st ed. (Morgan & Claypool Publishers, San Rafael, CA, 2007).

[18] J. J. Holmes, *Reduction of a Ship's Magnetic Field Signatures*, 1st ed. (Morgan & Claypool Publishers, San Rafael, CA, 2008).

[19] M. Norgren and S. He, "Exact and explicit solution to a class of degaussing problems," IEEE Trans. Magn. **36**, 308–312 (2000).

[20] D.-W. Kim, S.-K. Lee, B. Kang, J. Cho, W. Lee, C.-S. Yang, H.-J. Chung, and D.-H. Kim, "Efficient re-degaussing technique for a naval ship undergoing a breakdown in degaussing coils," J. Magn. **21**, 197–203 (2016).

[21] T. M. Baynes, G. J. Russell, and A. Bailey, "Comparison of stepwise demagnetization techniques," IEEE Trans. Magn. **38**, 1753–1758 (2002).

[22] L. Hasselgren and J. Luomi, "Geometrical aspects of magnetic shielding at extremely low frequencies," IEEE Trans. Electromagn. Compat. **37**, 409–420 (1995).

[23] M. Birsan and R. Tan, "The effect of roll and pitch motion on ship magnetic signature," J. Magn. **21**, 503–508 (2016).

[24] B. Froidurot, L.-L. Rouve, A. Foggia, J.-P. Bongiraud, and G. Meunier, "Magnetic discretion of naval propulsion machines," J. Magn. Magn. Mater. **242–245**, 1190–1194 (2002).

[25] B. Froidurot, L.-L. Rouve, A. Foggia, J.-P. Bongiraud, and G. Meunier, "Magnetic discretion of naval propulsion machines," IEEE Trans. Magn. **38**, 1185–1188 (2002).

[26] X. Brunotte, G. Meunier, and P. Bongiraud, "Ship magnetizations modelling by the finite element method," IEEE Trans. Magn. **29**, 1970–1975 (1993).

04 November 2023 19:11:03

[27] COMSOL Multiphysics® v. 6.0., www.comsol.com, COMSOL AB, Stockholm, Sweden, 2021.

[28] R. I. Joseph and E. Schlömann, "Demagnetizing field in nonellipsoidal bodies," J. Appl. Phys. **36**, 1579–1593 (1965).

[29] E. Schlömann, "A sum rule concerning the inhomogeneous demagnetizing field in nonellipsoidal samples," J. Appl. Phys. **33**, 2825–2826 (1962).

[30] W. F. Brown, Jr. and A. H. Morrish, "Effect of a cavity on a single-domain magnetic particle," Phys. Rev. **105**, 1198–1201 (1957).

[31] R. Moskowitz and E. Della Torre, "Theoretical aspects of demagnetization tensors," IEEE Trans. Magn. **2**, 739–744 (1966).

[32] S. Tandon, M. Beleggia, Y. Zhu, and M. De Graef, "On the computation of the demagnetization tensor for uniformly magnetized particles of arbitrary shape. Part I: Analytical approach," J. Magn. Magn. Mater. **271**, 9–26 (2004).

[33] S. Tandon, M. Beleggia, Y. Zhu, and M. De Graef, "On the computation of the demagnetization tensor for uniformly magnetized particles of arbitrary shape. Part II: Numerical approach," J. Magn. Magn. Mater. **271**, 27–38 (2004).

[34] A. Smith, K. K. Nielsen, D. V. Christensen, C. R. H. Bahl, R. Bjørk, and J. Hattel, "The demagnetizing field of a nonuniform rectangular prism," J. Appl. Phys. **107**, 103910 (2010).

[35] W. F. Brown, *Magnetostatic Principles in Ferromagnetism* (North Holland Publishing Company, Amsterdam, Netherlands, 1962).

[36] M. Sagawa, S. Fujimura, N. Togawa, H. Yamamoto, and Y. Matsuura, "New material for permanent magnets on a base of Nd and Fe (invited)," J. Appl. Phys. **55**, 2083 (1984).

[37] J. J. Croat, J. F. Herbst, R. W. Lee, and F. E. Pinkerton, "Pr–Fe and Nd–Fe-based materials: A new class of high-performance permanent magnets (invited)," J. Appl. Phys. **55**, 2078 (1984).

[38] See https://www.advancedmagnets.com for more information about sintered $Nd_2Fe_{14}B$ alloy.

[39] See https://mriquestions.com/magnetizing-metal.html for more information about magnetic saturation of ferromagnetic materials.

[40] D. Jiles, *Introduction to Magnetism and Magnetic Materials* (CRC Press, Taylor & Francis, Boca Raton, 1998).

[41] B. Heinrich, J. F. Cochran, M. Kowalewski, J. Kirschner, Z. Celinski, A. S. Arrott, and K. Myrtle, "Magnetic anisotropies and exchange coupling in ultrathin fcc Co(001) structures," Phys. Rev. B **44**, 9348–9361 (1991).

[42] B. Heinrich, S. T. Purcell, J. R. Dutcher, J. F. Cochran, and A. S. Arrott, "Structural and magnetic properties of ultrathin Ni/Fe bilayers grown epitaxially on Ag(001)," Phys. Rev. B **38**, 12879 (1988).

04 November 2023 19:11:03